JOURNAL OF GEOPHYSICAL RESEARCH, VOL. 115, B06309, doi:10.1029/2009JB006865, 2010

Characterization of fracture systems using precise array locations of earthquake multiplets: An example at Deception Island volcano, Antarctica

E. Carmona,[1] J. Almendros,[1,2] J. A. Peña,[1,3] and J. M. Ibáñez[1,2]

Received 8 August 2009; revised 5 December 2009; accepted 12 January 2010; published 17 June 2010.

[1] Volcano-tectonic earthquakes are common seismic events in active volcanic areas. The stress produced by volcanic processes is released through fracturing of the shallow crust. Very often, these earthquakes occur in multiplets with similar waveforms, a fact which indicates common source characteristics. In this work, we introduce a method that uses array techniques to calculate precise relative locations of earthquake multiplets. We use the relative slowness estimate method to determine accurately the apparent slownesses and propagation azimuths of the earthquakes relative to a selected master event. We also obtain precise estimates of the S-P delays. This information is used to calculate precise relative locations by ray tracing in an Earth model. We applied this method to determine the characteristics of the fractures activated during the 1999 seismic series at the Deception Island volcano, Antarctica. We selected a set of 17 earthquake multiplets, initially located in a small (4 × 4 km) region a few km NE of the array site. We estimated precise locations for 14 of the clusters. In most cases, hypocenters were distributed in well-defined planar geometries. We found the best fitting planes, which we interpreted as fractures in the medium. For two clusters, the method spatially separated the earthquakes into two subgroups. Thus, we obtained two planes for each of these clusters, resulting in a total of 16 fracture planes. This is the first time that the orientations of fracture planes related to a seismic series have been obtained using a seismic array. We performed several tests to check various aspects in relation to the stability of the method and concluded that the results were robust. The dip angles indicate that the planes are mostly subvertical, while the strike angles clearly show a NW-SE trend for most of the planes and a few planes with NE–SW trends. The geometry and position of these planes suggest that the 1999 seismic series was influenced by regional tectonics, although the origin of the destabilization of the system may be related to the reactivation of a shallow magma chamber.

Citation: Carmona, E., J. Almendros, J. A. Peña, and J. M. Ibáñez (2010), Characterization of fracture systems using precise array locations of earthquake multiplets: An example at Deception Island volcano, Antarctica, *J. Geophys. Res.*, *115*, B06309, doi:10.1029/2009JB006865.

1. Introduction

[2] The main objective of volcano seismology is to improve our knowledge of active volcanic systems through the analysis of the seismic signals that they generate. These signals contain information about many aspects of the volcano, for example parameters of the seismovolcanic source (position, geometry, dynamics, energy, spatiotemporal evolution, etc) and characteristics of the medium (velocity structure, attenuation, spatial distribution of heterogeneities, etc). Pure volcanic events such as volcanic tremors and long-period (LP) events provide insights into the mechanisms and dynamics of fluid transport within the volcanic system. In addition, volcano-tectonic (VT) events offer us an insight into the dynamics and geometry of brittle fractures in the medium, and thus constitute a powerful means of investigating the local state of stress produced by volcano dynamics [e.g., *Chouet*, 1996].

[3] Several tools can be used to achieve this objective. In volcanic regions the use of seismic arrays is very common as a complement to conventional seismic networks. The advantage of array techniques is that they provide a space-time sampling of seismic waves as they propagate across the array. These instruments are designed to estimate the apparent slowness vector, whose magnitude represents the inverse of the apparent velocity of the waves and whose direction

[1]Instituto Andaluz de Geofísica, Universidad de Granada, Granada, Spain.
[2]Also at Departamento de Física Teórica y del Cosmos, Universidad de Granada, Granada, Spain.
[3]Also at Departamento de Prehistoria y Arqueología, Universidad de Granada, Granada, Spain.

0148-0227/10/2009JB006865

indicates their propagation azimuth. Arrays allow us to analyze signals characterized by the absence of clear seismic phases, such as volcanic tremors, LP events, earthquake codas, and even seismic noise. They also allow us to analyze low-magnitude VT earthquakes that cannot be recorded properly at distances of more than a few km. These tasks would be difficult using seismic networks, although new methodologies based on seismic amplitudes have recently been developed and applied to source location of LP seismicity [e.g., *Battaglia et al.*, 2005].

[4] Array techniques have been used to locate seismic events, investigate the temporal evolution of the source, analyze the characteristics of seismic noise, and study the details of the local structure. They have been applied at volcanoes such as Stromboli [*Chouet et al.*, 1997; *La Rocca et al.*, 2004], Etna [*Saccorotti et al.*, 2004], Vesuvius [*Saccorotti et al.*, 2001b], Teide [*Del Pezzo et al.*, 1997; *Almendros et al.*, 2000, 2007], Masaya [*Métaxian et al.*, 1997], Arenal [*Métaxian et al.*, 2002; *Mora et al.*, 2006], Kilauea [*Almendros et al.*, 2001a, 2001b], Copahue [*Ibáñez et al.*, 2008], and Colima [*Palo et al.*, 2009]. The use of array techniques to obtain spatial locations is based on three different approaches: circular wavefronts; ray tracing; and joint location with various arrays. The first method is based on the estimate of the radius of curvature of the wavefront, and implicitly assumes nearby sources [*Almendros et al.*, 1999]. The second uses ray tracing in a predefined Earth model. In addition to the information on the apparent slowness vector provided by the array, we need to know the arrival times of P and S phases to determine the distance along the seismic ray. This requirement means that the technique can only be applied to earthquakes with clear phases [e.g., *Del Pezzo et al.*, 1997; *Almendros et al.*, 2000, 2007; *Saccorotti et al.*, 2001b]. Finally, the third method is based on the use of several arrays. The apparent slowness vectors obtained from each array are combined to determine the spatial position of the source. This method is powerful and flexible, and can be applied to any type of earthquake, including pure volcanic signals [*Almendros et al.*, 2000, 2001a, 2001b; *La Rocca et al.*, 2000, 2008; *Métaxian et al.*, 2002].

[5] In any case, the source locations obtained with either seismic arrays or seismic networks are associated with a degree of uncertainty caused by various factors, some of which are related to the methodology selected. For example, for array analyses there is an error introduced by the approximation of the signals to plane wavefronts, the configuration of stations in the array, the slowness grid size and spacing, etc. For seismic networks, there are errors related to the phase picking, position of the stations, etc. On top of that, in both cases we find the effect of natural factors such as the heterogeneities of the velocity structure (that produce path and site effects), and the presence of seismic noise. The uncertainty intervals are relatively large, which produces generally low-accuracy hypocentral locations.

[6] However, there are methods that in some cases allow us to obtain accurate locations. An example is the relative location of similar earthquakes. This method relies on the observation that seismic series contain earthquakes with very similar waveforms. This similarity is due to the fact that the earthquakes originate along the same fault plane and therefore share similar source mechanisms and hypocenter locations [*Tsujiura*, 1983; *Geller and Mueller*, 1980]. If these conditions were not met, we would see waveform differences due to the different mechanisms and locations (different P and S waveforms and travel times, distinct path effects, etc). Comparison of the seismograms produces the grouping of earthquakes into clusters characterized by high waveform similarity. Within each cluster, we can take advantage of this similarity to refine the phase picks and perform precise relative locations [*Poupinet et al.*, 1984; *Maurer and Deichmann*, 1995].

[7] Relative locations using network data have been obtained in tectonic and volcanic regions. In tectonic areas this technique is mainly used to gather information about the plane of rupture when focal mechanisms cannot be calculated, e.g., for the analysis of series of microearthquakes [*Deichmann and García-Fernández*, 1992; *Stich et al.*, 2001; *Saccorotti et al.*, 2002; *Scarfi et al.*, 2003; *Massa et al.*, 2006; *Ruiz et al.*, 2006; *Ocaña et al.*, 2008; *Carmona et al.*, 2009]. Recently, relative locations have been used for the study of nonvolcanic tremors [*Shelly et al.*, 2009]. In volcanic regions, absolute locations of VT earthquakes are particularly complicated because of the heterogeneity of the environment, the low magnitude of the events, the difficulty of establishing seismic networks with good coverage, etc. The relative location technique provides detailed information on the distribution of hypocenters of VT earthquakes. This enables us to define the extent and the geometry of active magmatic systems [*Frémont and Malone*, 1987; *Gillard et al.*, 1996; *Jones et al.*, 2001; *Musumeci et al.*, 2002; *Alparone and Gambino*, 2003; *Brancato and Gresta*, 2003; *Battaglia et al.*, 2004; *Hensch et al.*, 2008]. It has also been applied to the analysis of temporal changes that occur in volcanoes as a result of internal dynamics and movements of magma [*Ratdomopurbo and Poupinet*, 1995; *Snieder and Hagerty*, 2004; *Pandolfi et al.*, 2006; *Carmona et al.*, 2007; *Martini et al.*, 2009].

[8] In this paper, we combine relative locations and array techniques. We develop a method based on the work of *Almendros et al.* [2004] that allows for the precise relative locations of microearthquakes recorded by a seismic array. The use of arrays ensures that we could apply the method even to earthquakes that are too small to be analyzed with conventional networks. We analyze a series of VT earthquakes that occurred in Deception Island, Antarctica, in 1999 [*Ibáñez et al.*, 2003b]. We compare the waveforms to select clusters of similar earthquakes. We obtain accurate estimates of the relative apparent slowness vectors and S-P delays and spatially locate the earthquake sources. The observed distributions of hypocenters fit to a plane, which we interpret as the rupture plane responsible for the generation of earthquakes. To check the robustness of the method, we perform a series of tests to confirm its validity for finding rupture planes with array techniques. Finally, we discuss the results in the regional tectonic and volcanic environment of Deception Island.

2. Tectonic Setting

[9] Deception Island is one of the South Shetland Islands, lying 62° 43′S and 60° 57′W off the Antarctic Peninsula. Its regional tectonic framework is quite complex due both to its position in the Bransfield Strait, between the Antarctic

Peninsula and the South Shetland Islands, and to the converging of several tectonic plates [*Pelayo and Wiens*, 1989; *Baraldo and Rinaldi*, 2000; *Robertson Maurice et al.*, 2003]. These tectonic plates are represented by two major plates, the South American Plate and the Antarctic Plate, and three microplates, the Scotia, the Drake and the South Shetland (Figure 1).

[10] The South Shetland Islands trench is attributed to a slow slab rollback subduction process [*Ibáñez et al.*, 1997; *Robertson Maurice et al.*, 2003] which led to the breakup and separation of the South Shetlands microplate from the Antarctic Peninsula, 2 Myr ago, creating the well-known Bransfield Rift. In addition to normal faults, this rift also has three active extensional NE trending basins and is related to the volcanic activity in the area. The shallow regional seismicity (above 40 km) is consistent with the extension of the rift, while the deepest seismicity is consistent with the subduction of the Drake plate [*Pelayo and Wiens*, 1989; *Ibáñez et al.*, 1997; *Robertson Maurice et al.*, 2003].

[11] Deception Island is located on the extension axis of the Central Bransfield Basin and is probably one of the most active volcanoes in Antarctica. Several volcanic eruptions have been reported in 1842, 1912, 1917, and more recently in 1967, 1969 and 1970 [e.g., *Smellie*, 1988]. The island has a horseshoe shape with a flooded caldera and its emerged area is about 15 km in diameter. The origin of this peculiar morphology has several possible explanations. It may have been produced by the collapse of a large caldera due to powerful eruptions, which filled up and produced a ring-shaped fracture system [*González-Ferrán and Katsui*, 1970; *Baker et al.*, 1975]. Another possible explanation could be that the caldera was formed by a depression caused by extensive tectonic movements along normal faults governed by a regional extensional trend, so ruling out previous findings as to the presence of circular faults [*Martí et al.*, 1996; *Rey et al.*, 1995; *González-Casado et al.*, 1999]. Moreover, tomographic models for the region image a high-velocity structure NW of Deception Island. This structure extends NE–SW parallel to the axis of the Bransfield Rift. It has been interpreted as the basement of the South Shetland Islands [*Zandomeneghi et al.*, 2009], which supports the importance of the regional tectonics in the origin and evolution of Deception Island.

[12] Three major fault systems were identified in this zone from field observations and seismic reflection data [*Rey et al.*, 1995; *Martí et al.*, 1996]. The first major system is consistent with the extensional tectonic regime of the Bransfield Strait, with a NE–SW direction. These alignments are consistent with the eruptions of 1967 and 1970. The second system presents an approximately EW direction and coincides with various different alignments including the alignments of Mt. Kirkwood, the phreatomagmatic eruptions produced by these fissures and the alignments of submarine cones inside the caldera. The third system is NNW–SSE oriented and its main evidence is in the Costa Recta alignment [*Fernández-Ibáñez et al.*, 2005]. Other alignments can be observed in the Mt. Pond system faults, in the subparallel faults present throughout the Fumarole Bay and the Black Glacier, and in the eruptive fissures of 1969. In addition, geological surface observations, geophysical data, bathymetric information, digital elevation models, morphological evidence of volcanic recent activity, etc, show the presence of a wide variety of fault systems and evidence the complexity of Deception Island [*Martí et al.*, 1996; *González-Casado et al.*, 1999; *Paredes et al.*, 2006; *Maestro et al.*, 2007; *Barclay et al.*, 2009].

3. Seismicity of Deception Island

[13] In recent years Deception Island has been monitored from the perspective of several different geophysical disciplines (seismology, geochemistry, geodesy, gravimetry) in Austral summer surveys. The recent eruptions, the presence of two Antarctic bases, and the massive arrival of tourism, underline the importance of detailed studies and monitoring of its seismovolcanic activity.

[14] Systematic monitoring of seismic activity in the island began in the 1950s. This first stage ended in the late 60s, when the most recent eruptions occurred. There is written evidence to the effect that there was a considerable increase in seismic activity in the area just before the eruptions [*Valenzuela et al.*, 1968]. After the 1970 eruption, Deception Island was not monitored again until the Austral summer of 1987. Since then, local volcano-tectonic earthquakes and even some tremor episodes have been recorded. These records, obtained by vertical component seismometers, enabled the first seismic studies of the island to be carried out [*Vila et al.*, 1992, 1995]. In the 1991–1992 survey a considerable increase in activity was noted [*Ortiz et al.*, 1997]. Between 1994 and 1999 several seismic arrays were deployed in order to locate LP events and volcanic tremors [*Almendros et al.*, 1997, 1999; *Ibáñez et al.*, 2000]. Since 1998, a variety of seismic instruments have been used, including seismic arrays, short-period stations and broadband stations. The monitoring of activity has usually been carried out during Austral summers. A permanent broadband station that allows researchers to obtain a continuous record was only deployed in January 2008 [*Martínez-Arévalo et al.*, 2009].

[15] Since the start of the monitoring surveys in Deception Island, the level of seismic activity has been variable. Periods of very low activity were often followed by others of substantially higher activity. Two maxima (in 1992 and 1999 [see *Ibáñez et al.*, 2003a]) were considered of sufficient importance to be classified as seismic series. Some characteristics of these two series were similar (i.e., magnitude distribution, felt earthquakes). Until 1992 LP events predominated over VT earthquakes. In the 1992 series 766 VT earthquakes occurred during a 2 month period, including some felt events [*Ortiz et al.*, 1997]. After this VT series the LP events started predominating over the VTs again. Between 1993 and 1998 seismic activity returned to its normal parameters, with variable activity levels [*Ibáñez et al.*, 2003a]. The second remarkable reactivation chapter took place during the 1998–1999 survey, when a total of 3643 events were recorded. In both episodes the considerable increase in activity was probably due to a magmatic intrusion that did not reach the surface, causing local tectonic destabilization [*Ortiz et al.*, 1997; *Ibáñez et al.*, 2003a]. In the next survey (1999–2000) several dozen VT events were registered, some of which were located in the same epicentral area as the January–February 1999 earthquakes. These events might correspond to the activation of the same fracture systems and could be related to the

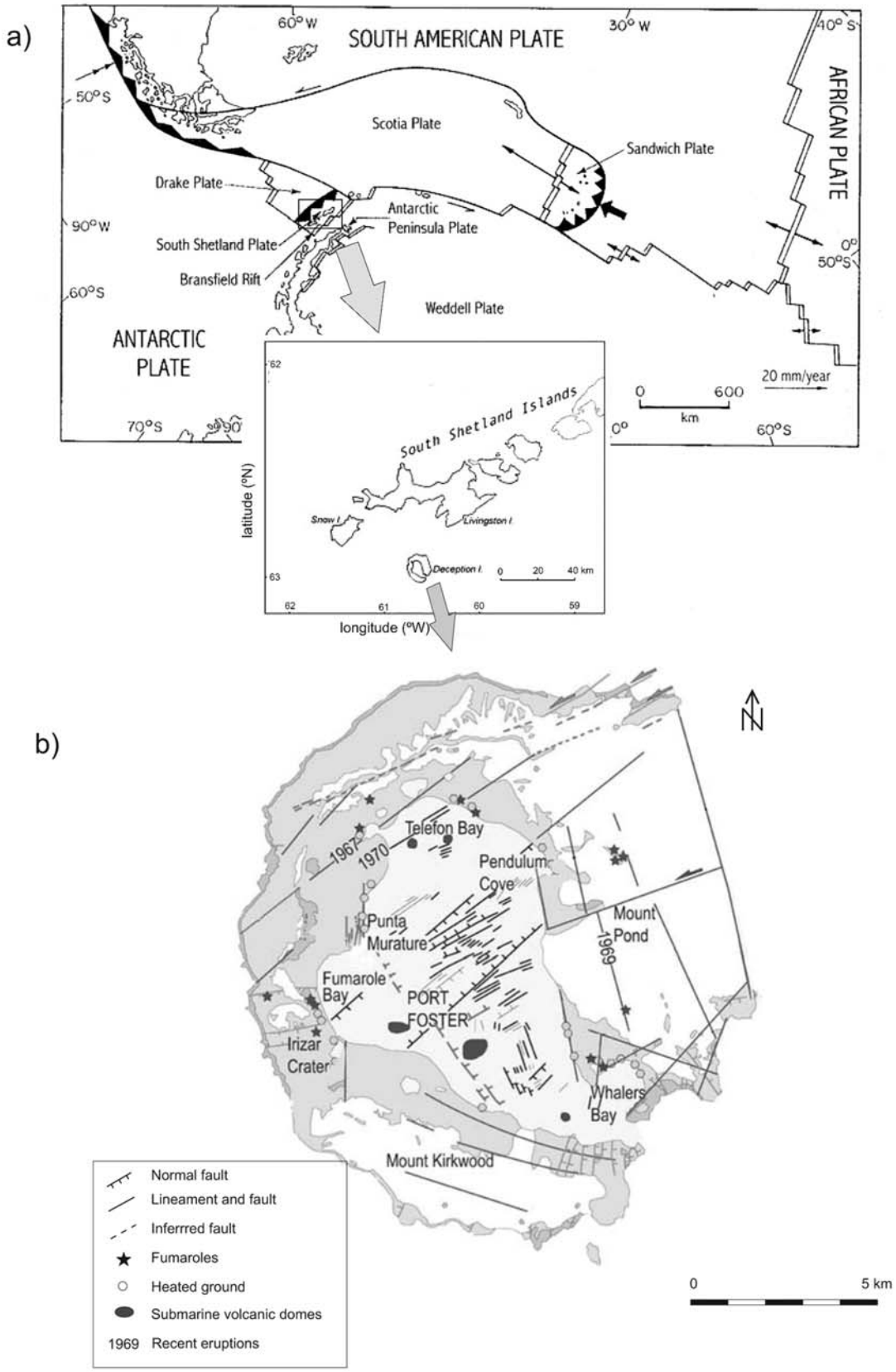

Figure 1. (a) Tectonic map of the Scotia region. The inset shows a map of the South Shetland Islands region. (b) Simplified geological map of Deception Island (modified from *Maestro et al.* [2007], copyright 2004, with permission from Elsevier).

destabilization caused by the magmatic intrusion that produced the series. Some VT earthquakes, LP events, and volcanic tremor episodes occurred in the other annual surveys until February 2009, although the level of activity has been in general much lower.

4. Instruments

[16] During the 1998–1999 Antarctic survey two seismic arrays were deployed, each of which was composed by two 8-channel, 16-bit data acquisition modules. Every acquisition module was controlled by a notebook PC through its parallel port. Synchronization and management of time, one of the key factors in a seismic array system, was based on GPS receivers, in which the configuration and control was managed through the PC's serial port in RS-232 format. A sampling rate of 200 samples per second was used. Data were recorded in hard disks by the data acquisition systems, using a STA/LTA trigger algorithm. All the stations were equipped with 4.5 Hz Mark L28 sensors, whose response was extended electronically to 1 Hz. The first seismic array, located in the Obsidianas Beach, was composed of 1 three-component and 13 vertical component stations. The second seismic array, located in Fumarole Bay, was composed of 7 vertical Mark L28 sensors (also extended to 1 Hz) and 3 three-component stations with 1 Hz Mark L4C sensors. Two continuous recording stations were also deployed, equipped with three-component Mark L4C seismometers controlled by a 16 bit data acquisition system. They were located in the vicinity of the Spanish Base and in the northern Fumarole Bay area.

[17] The spatial distribution of the sensors in the array systems was originally conceived with two goals in mind. First, we sought to compare the seismic activity in both areas; and second we wanted to determine the source position by applying a joint location technique [*La Rocca et al.*, 2000; *Almendros et al.*, 2000]. In the end, this second objective proved unfeasible, due to the great difference in the shallow velocity structure under both arrays, which seriously affected the estimates of the slowness vector [*Saccorotti et al.*, 2001b]. Taking into account the extremely complex lateral structure beneath the Obsidianas array [*Saccorotti et al.*, 2001a; F. Luzón et al., Shallow structure of Deception Island volcano, Antarctica, using the two station spatial autocorrelation method on a dense set of seismic arrays, submitted to *Geophysical Journal International*, 2009], and following *Ibáñez et al.* [2003b], we decided to consider only data recorded in the Fumarole array. This seismic array was deployed in the neighborhood of the fumarolic system of Fumarole Bay, 500 m N–NE from the Argentinean Base. Its shape was approximately a double concentric semicircle, with radii of 60 m and 120 m, thus giving a total aperture of 240 m. The angular separation between stations was approximately 45° in the inner semicircle and 60° in the outer one (see Figure 2).

5. The 1999 Seismic Series

[18] The 1999 seismic series at Deception Island volcano began in late December 1998. The arrays were recording from the beginning of the series until the end of February 1999. At that point we had to remove the arrays, although other instruments continued recording until April 1999, when the onset of winter prevented us from obtaining more data and finding out exactly when the series really ended [*Ibáñez et al.*, 2003b]. The Fumarole array recorded a total of 3643 events of which 2072 were VT earthquakes; 1556 events were LP events; and 15 were hybrids. There were also a few episodes of volcanic tremor. The moment magnitude of the VT earthquakes ranged between −0.8 and 3.4. The largest earthquakes in this series, with magnitudes of 2.8 and 3.4, occurred on 11 and 20 January 1999, respectively, and were felt by the staff at the "Gabriel de Castilla" Antarctic Station. With the exception of these two large earthquakes, the magnitude distribution and seismic energy release as a function of time is approximately constant throughout the series. The series was characterized by low stress drop values between 0.1 and 4 bar [*Havskov et al.*, 2003]. Source sizes were estimated to be in the order of 10–100 m [*Ibáñez et al.*, 2003b]. These results indicate that the fractures involved in the process of generating the series were probably quite small.

[19] *Ibáñez et al.* [2003b] calculated source locations for 863 VT earthquakes. They used the zero-lag cross-correlation (ZLCC) technique [*Frankel et al.*, 1991; *Del Pezzo et al.*, 1997] to estimate the slowness vectors of the P wave arrivals at three frequency bands. The S-P differences were estimated visually. Subsequently, they obtained the hypocenters using ray tracing. The velocity model was a combination of models used by previous authors [*Ibáñez et al.*, 2000; *Saccorotti et al.*, 2001a]. Locations show that the majority of these VT events were located very close to the array site and at depths of around 2 km. Two alignments can be inferred, one at a direction of N45°E, with focal depths of between 1 and 4 km and a second, more dispersed alignment, which extends N80°E (Figure 2). *Ibáñez et al.* [2003b] also analyzed LP events and volcanic tremor episodes, obtaining azimuth and slowness values quite different from those obtained for the VTs. These results indicate that the 1999 LP seismicity is unrelated to the VT series, and agree with previous research in different surveys [*Almendros et al.*, 1997, 1999; *Ibáñez et al.*, 2000] suggesting that the LP seismicity has a hydrothermal origin. We analyzed 9 hybrid events and obtained similar results to those obtained for VT events, which indicates the presence of fluids in the VT source area.

[20] Our work is based on the set of VT earthquakes recorded in the Fumaroles array and located by *Ibáñez et al.* [2003b]. These locations allowed the authors to carry out a preliminary analysis of the series. However, the uncertainties of the locations are too large to obtain the planes associated with the earthquake generation processes; hence the need for a method of relative location to calculate the hypocenters with greater precision using array techniques.

6. Search for Clusters

[21] The first step in a precise relative location is to try to detect clusters of earthquakes with similar waveforms. We selected the central station of the Fumarole array (Figure 2) to search for these clusters. Figure 3 shows an example of three-component seismogram for a sample VT earthquake. Traces were band-pass filtered between 4 and 15 Hz using a zero-phase, three-pole Butterworth filter. For each trace we

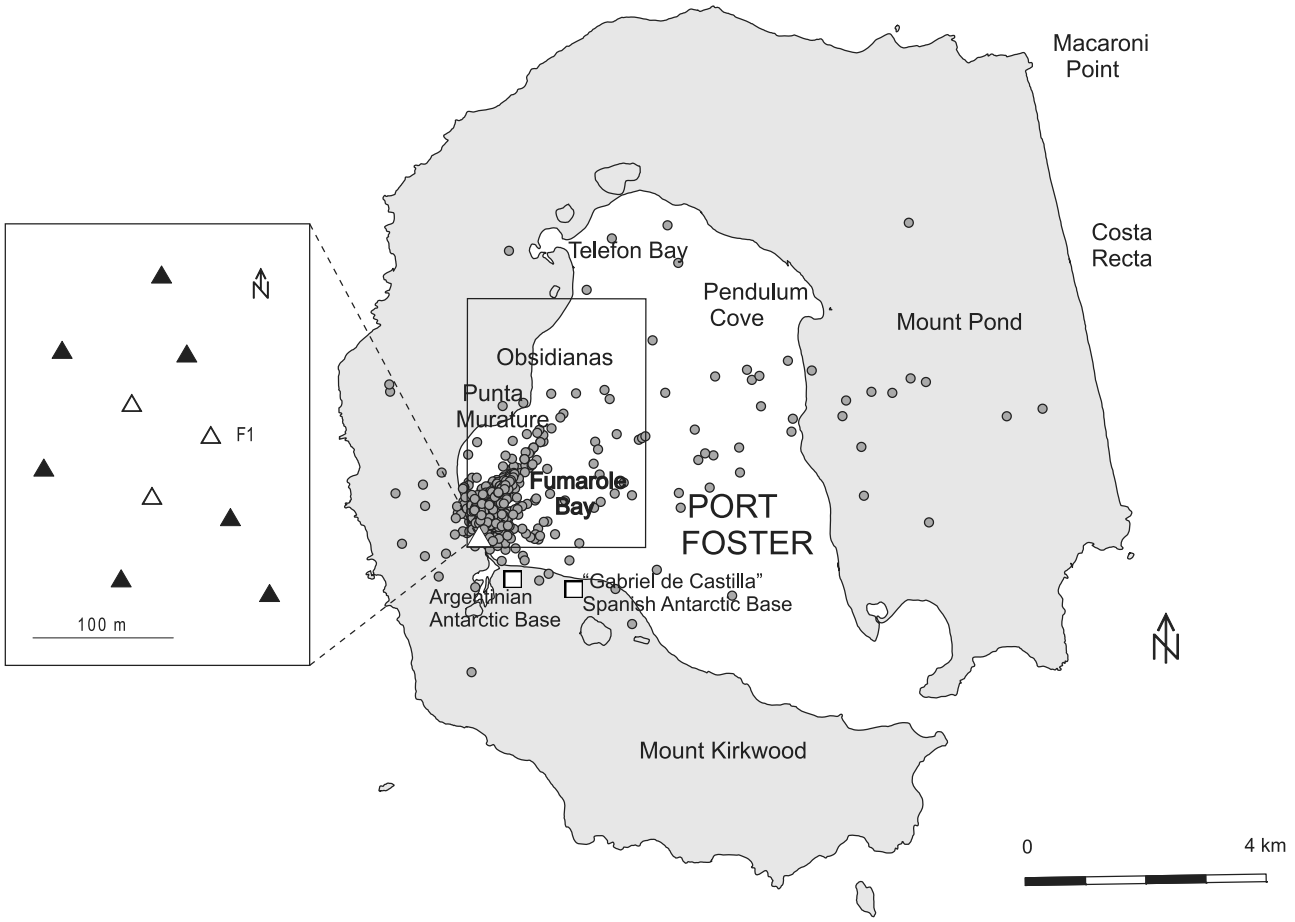

Figure 2. Preliminary epicentral locations of the VT earthquakes of the 1999 seismic series at Deception Island volcano, showing the location and configuration of the seismic antenna used for the present analysis. In the close-up, black triangles correspond to vertical stations, while the open triangles correspond to three-component stations. F1 is the central station of the array, used for the correlation analysis (see section 6 for explanations). The box in the epicentral region corresponds to the area zoomed in Figures 7, 8, and 11.

selected a window of 120 samples (0.6 s), starting 0.1 s before the arrival times picked for the P and S waves. The initial and final 10% of the window were smoothed using a cosine window. We calculated the cross correlations for the P wave (vertical component) and for the S wave (N–S component) of the 863 located earthquakes. The result was a correlation matrix for the P wave and another for the S wave of all the events located in the series. With the two cross-correlation matrices, we performed a cluster search using the equivalence class technique [*Press et al.*, 1989; *Aster and Scott*, 1993]. We used three parameters to define events with a similar waveform: A first threshold for the cross correlation of the S wave, a second threshold for the cross correlation of the P wave, and a third threshold that refers to

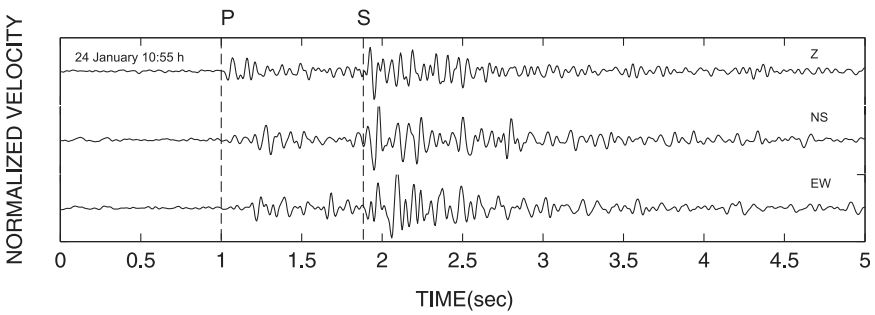

Figure 3. Three-component seismogram for a sample earthquake recorded at station F1 (see Figure 2). The dashed lines correspond to the arrivals of the P and S waves. Data have been filtered between 1 and 30 Hz.

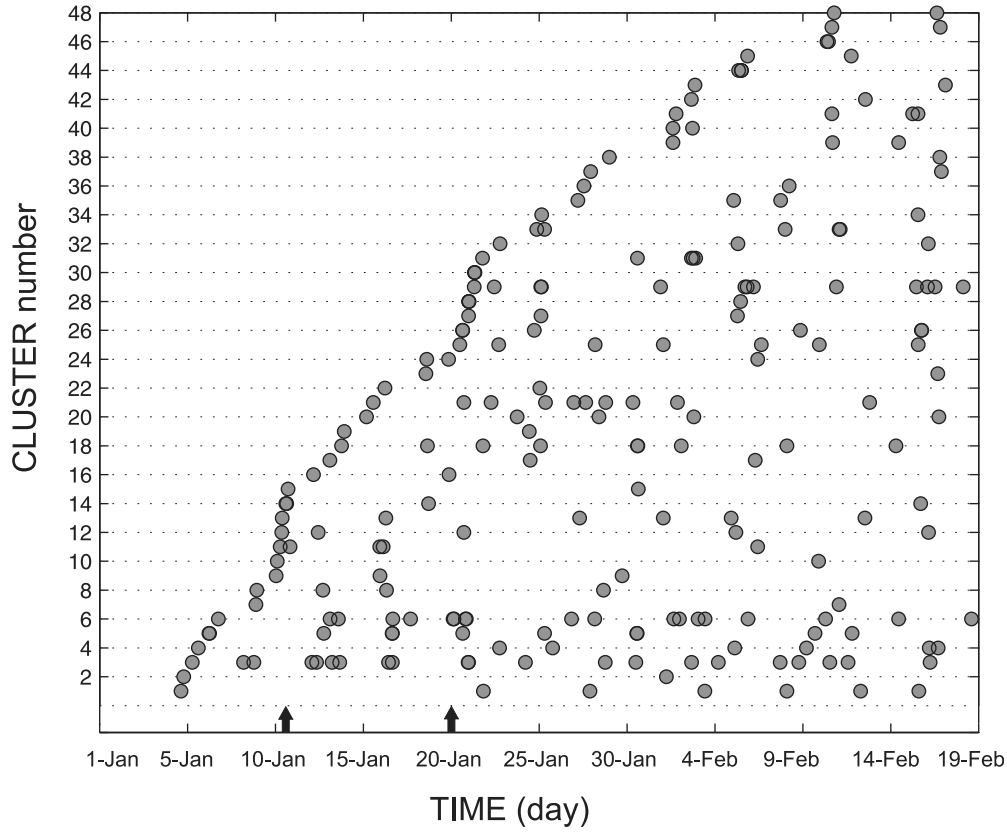

Figure 4. Temporal distribution of the earthquakes included in the 48 multiplets identified. At the bottom, the occurrences of two earthquakes with $M_w > 2.8$ (not included in the clusters) are indicated with black arrows.

the standard scalar product of the corresponding rows of the correlation matrix of the S wave. This last threshold was used to ensure that each event had similar correlations within the same family, thus rejecting accidental cases [*Maurer and Deichmann*, 1995]. The thresholds used in our work were 0.9 for the correlation of S wave, 0.9 for the P wave and 0.5 for the scalar product of the S wave. These correlation thresholds are quite high, which ensures a very good similarity in the waveforms. A total of 48 clusters were found, including 19 doublets, 9 triplets, and 20 multiplets with four or more events. The temporal distribution of these clusters (Figure 4) shows that they were spread over time, that is, the earthquakes within the clusters occur along the whole recording period. It can also be seen that there was no time gap in the occurrence of clusters. In total, 225 events were grouped, which represents 26% of the total number of volcano-tectonic events located in the series. This percentage is fairly representative of the series given the low magnitude of the events. The vast majority are in a magnitude range of 0–1 M_w. The clusters present very different waveforms (Figure 5), which suggests a diversity of source mechanisms.

7. Precise Relative Locations

[22] The occurrence of earthquakes with similar waveforms (multiplets) requires similar source and path effects. Therefore multiplet earthquakes must share similar source locations and mechanisms. Under this assumption, the main differences observed within a multiplet are just phase delays due to the slightly different lengths of the raypaths. These ideas constitute the basis of the master event relative location method.

[23] In our case, the earthquakes were recorded by a seismic array instead of a distributed network. Techniques based on differences of travel times cannot be applied. A seismic array is a tool to estimate the apparent slowness vectors, and thus apparent slowness and azimuth are the parameters that should be used.

[24] *Almendros et al.* [2004] introduced a technique that combines relative location and array analysis. Their relative slowness estimate (RelSE) method compares the waveforms of similar earthquakes recorded by a seismic array to estimate precisely the differences of apparent slowness and propagation azimuth of wavefronts corresponding to the same phase. This information can be used to produce accurate source locations, as will be shown below.

[25] Among the set of VT clusters found in the 1999 seismic series at Deception Island volcano, we selected 17 clusters with five or more members. For each cluster, we chose the event with the best signal-to-noise ratio as the master event.

7.1. Initial Source Relocations

[26] The preliminary location performed by *Ibáñez et al.* [2003b] was based on a systematic application of the

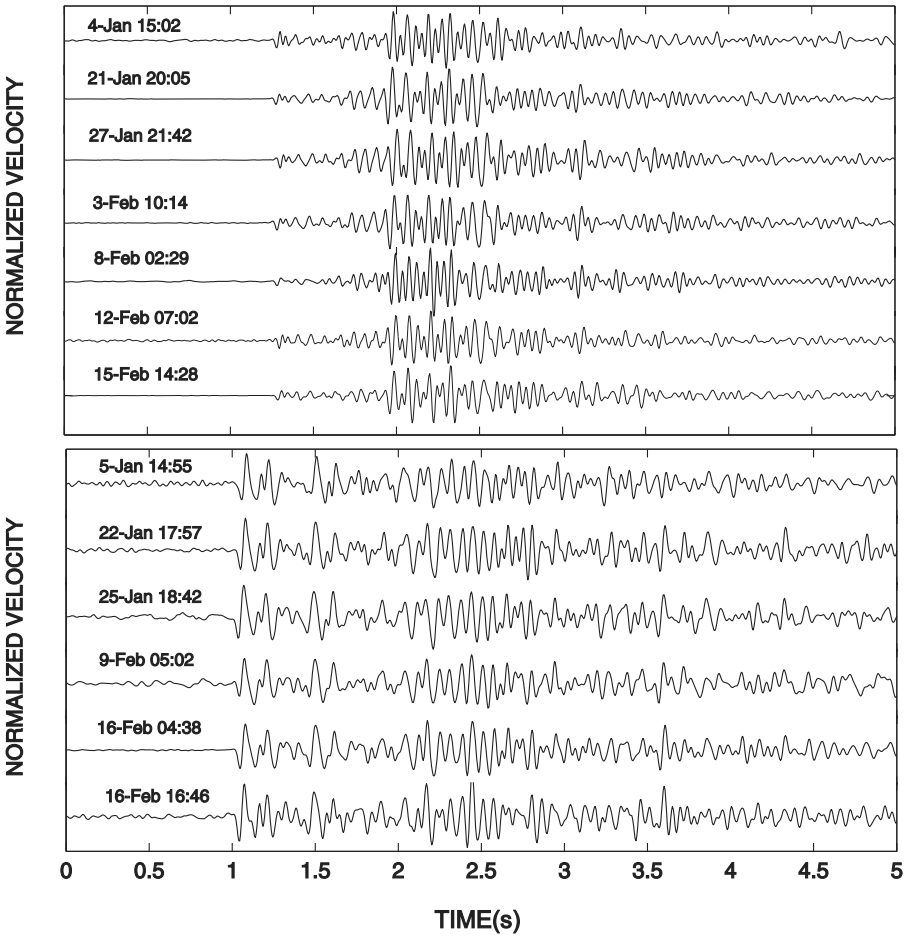

Figure 5. Examples of vertical component seismograms for two earthquake clusters (1 and 4) recorded at station F1. Data have been filtered between 1 and 30 Hz and aligned at the P arrival.

ZLCC method. They used different filters, analysis windows of 60–80 samples, an overlapping of 50% of the window length, and extended the analysis to the full seismogram from the preevent noise to the coda. This procedure ensures the fast and automated estimate of a consistent solution, within the uncertainty range, for the apparent slowness vector of the P wave of each VT earthquake.

[27] However, *Ibáñez et al.* [2003b] do not examine whether theirs is the best possible estimate. In fact, we observed that the results of *Ibáñez et al.* [2003b] for the VT clusters displayed a relatively large dispersion, even though the waveforms within each cluster were similar. For this reason, we started our analysis by reestimating the apparent slowness vectors using the ZLCC method. We fine-tuned the parameters to ensure that the estimates were made using exactly the same segments of seismogram around the P wave arrivals. We selected a filter in the 4–12 Hz band and a window length of 40 samples; increased the overlapping of successive windows to 95% of their length; and reduced the apparent slowness grid interval to 0.01 s/km. We also made a new picking of the P and S wave arrivals to estimate the S-P delay.

[28] With the results of this procedure, we calculated hypocenter locations using ray tracing. The model selected to represent the medium is similar to that used by *Ibáñez et al.* [2003b]. It is a combination of 1-D Earth models used in previous works. The base was the model described by *Ibáñez et al.* [2000] for the whole island. This was merged with the model calculated by *Saccorotti et al.* [2001a] for the shallow layers of Fumarole Bay. We used a Poisson ratio of 0.25 (which implies a Vp/Vs ratio of 1.73). To smooth the model and avoid discontinuities and critical reflections, we calculated an exponential fit of the form $v(z) = A - B*\exp(-z/C)$, where z is the depth, and A, B, and C are constants. The values obtained for these constants are A = 6 km/s, B = 5.1 km/s, and C = 2.5 km.

[29] Figure 6a shows the epicentral distribution of the master events. The remaining members of the multiplets are located near their master, and have not been plotted so as to ensure greater clarity. We can see two alignments of hypocenters at 35° and 70°N. These trends coincide approximately with the alignments at 45° and 80°N found in the preliminary analysis of the series [*Ibáñez et al.*, 2003b]. The coincidence suggests that the clusters are a good representation of the whole series. We estimated the location error quantitatively using (1) the size of the region corresponding to an uncertainty of 90% for each estimate of the apparent slowness vector with the ZLCC method and (2) the uncertainty associated with the determination of the S-P delays. These parameters provide spatial uncertainty intervals of around 0.5 km in horizontal and 1 km in vertical for most of the master events. These errors are similar to those estimated

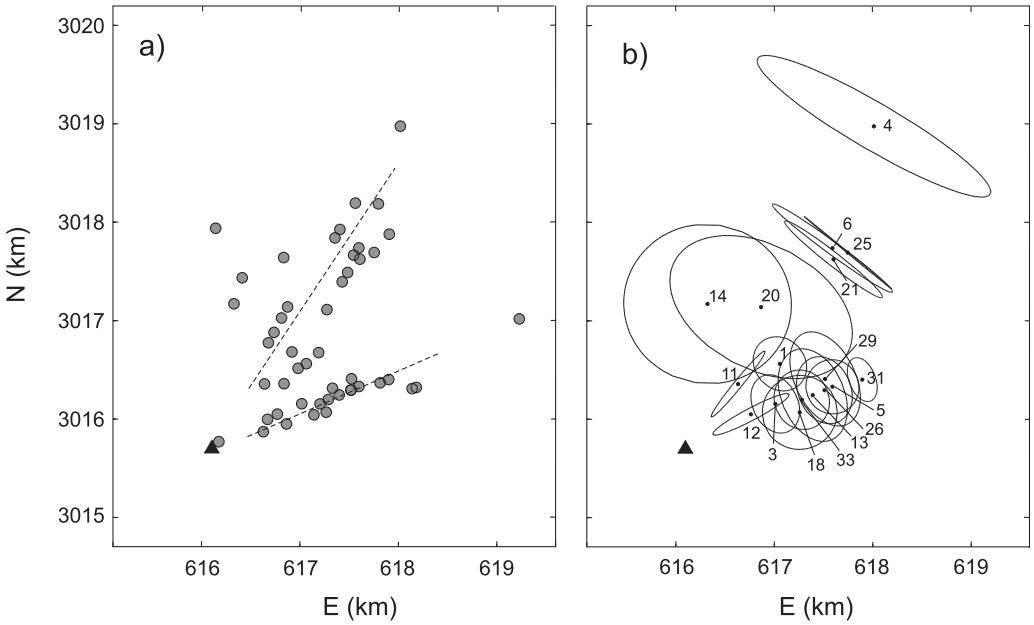

Figure 6. (a) Relocated epicentral map for master events of all clusters of the series. The dashed lines indicate two possible epicenter alignments. (b) Error ellipses (90% confidence regions) of the locations of the master events of the clusters analyzed. The black triangle marks the position of the array.

by *Ibáñez et al.* [2003b]. Figure 6b shows the horizontal projections of the error regions for the master events of the clusters with five or more elements.

7.2. Application of the RelSE Method

[30] Once we had identified and relocated the VT earthquake clusters, we applied the RelSE method [*Almendros et al.*, 2004]. This method uses array data to provide a precise estimate of the relative apparent slowness vectors of the events of the cluster with reference to the absolute apparent slowness vector of a master event. The innovation introduced by the RelSE method relies on the following. The time delay between the arrivals of a wavefront from an earthquake n to two array stations i, j is given by:

$$\Delta t_{ij}^{n} = \Delta \mathbf{r}_{ij} \cdot \mathbf{s}_{n} \tag{1}$$

where $\Delta \mathbf{r}_{ij}$ represents the position vector of the j station from the i station, and $\mathbf{s}_n$ is the apparent slowness vector that characterizes the propagation of the wavefront. Classic array techniques are based on the comparison of the seismograms among the array stations. Several methodologies can be used, but in all cases they allow for the calculation of the delays Δt_{ij}^{n} and the estimate of the apparent slowness vector $\mathbf{s}_n$. The accuracy of the estimate depends on our ability to measure accurate time delays. But in many situations the delays cannot be determined precisely, since site effects may produce important waveform variations between the stations of the array.

[31] Let us suppose now that two earthquakes m, n are recorded at the same array. The difference of delays of the same phase at two stations i,j is given by:

$$\Delta t_{ij}^{n} - \Delta t_{ij}^{m} = \Delta \mathbf{r}_{ij} \cdot \Delta \mathbf{s}_{mn} \tag{2}$$

where $\Delta \mathbf{s}_{mn} = \mathbf{s}_n - \mathbf{s}_m$ is the difference between the apparent slowness vectors corresponding to the earthquakes. This difference of delays can be also written as:

$$\Delta t_{ij}^{n} - \Delta t_{ij}^{m} = \Delta t_{j}^{mn} - \Delta t_{i}^{mn} \tag{3}$$

where Δt_i^{mn} represents the delay between the arrival times of a phase of earthquake n and the same phase of earthquake m at station i of the array. Combining equations (2) and (3), we obtain the expression:

$$\Delta t_{j}^{mn} - \Delta t_{i}^{mn} = \Delta \mathbf{r}_{ij} \cdot \Delta \mathbf{s}_{mn} \tag{4}$$

It may seem that this equation adds nothing to the problem, compared to equation (2). However, in the case of clusters of similar earthquakes recorded at a seismic array, the differences Δt_i^{mn} can be determined more accurately than the differences Δt_{ij}^{n}. In other words, we can calculate the delay between the arrivals of two earthquakes to the same station more precisely than the delay between the arrivals of a single earthquake to two array stations. This is a consequence of the improved waveform similarity observed among multiplet earthquakes [see, e.g., *Almendros et al.*, 2004, Figure 14].

[32] The RelSE method uses equation (4) to determine precisely the relative apparent slowness vector for earthquakes with similar waveforms recorded by a seismic array. We define a function that represents the inverse of the least squares misfit between the measure $\Delta t_j^{mn} - \Delta t_i^{mn}$ and a plane wavefront. The best estimate of the relative slowness vector is obtained by maximizing this function.

[33] We apply the RelSE method to the P wave for the selected earthquakes. The parameters we use are based on the results of the tests described by *Almendros et al.* [2004]. We also performed several tests to search for the optimum parameters for our analysis. We filtered the data in the 4–

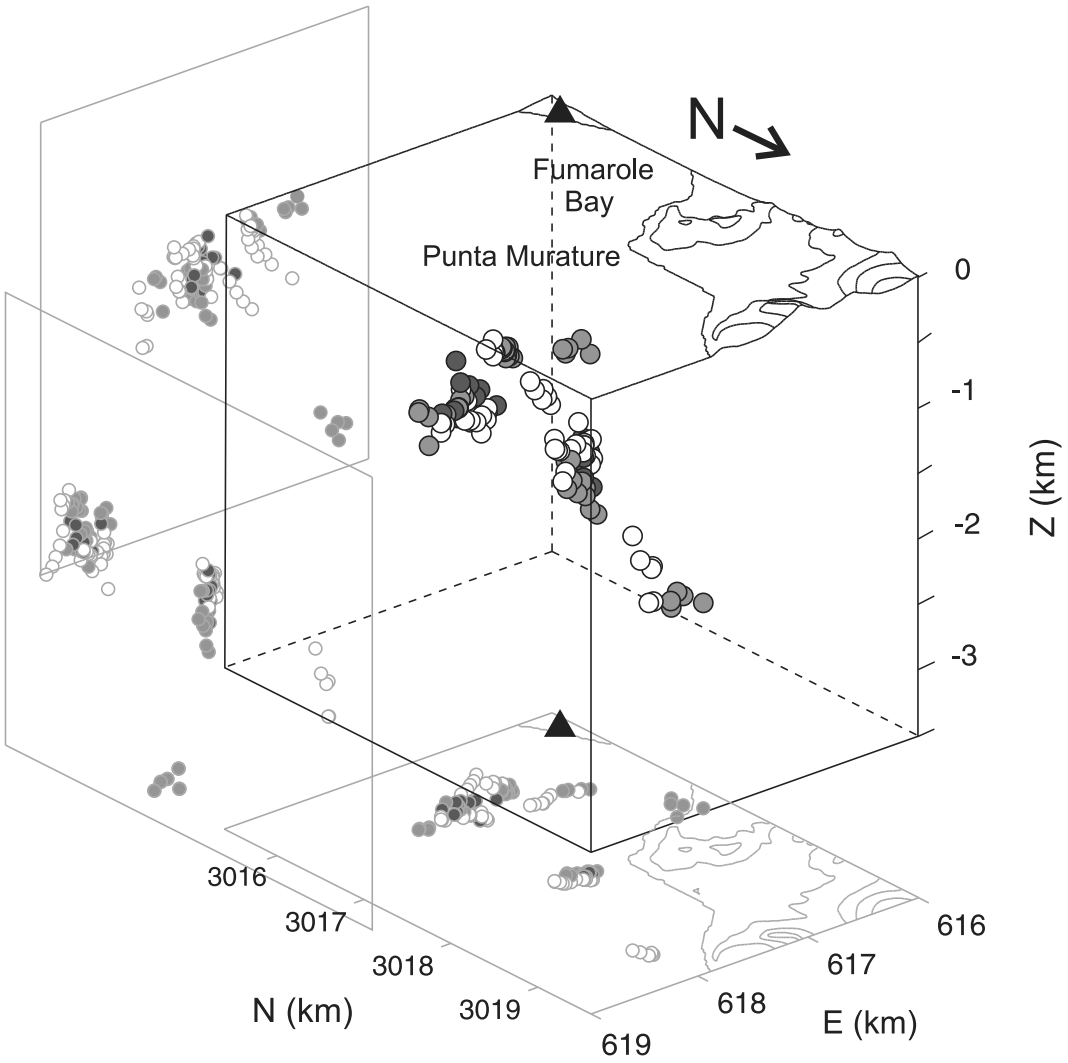

Figure 7. Summary of relative source locations for the 16 clusters selected. Each cluster is shown in a different shade of gray. Side and bottom planes contain vertical and horizontal projections of the hypocenters. The triangle marks the position of the array.

12 Hz band using a two-pole, zero-phase Butterworth filter. These parameters represent a compromise between the needs to reduce undesired noise and to minimize waveform distortion. The duration of the analysis window is 0.2 s (40 samples). This ensures that we use at least 2–3 periods of the signal. Larger windows involve the analysis of larger portions of the P wave coda, which do not necessarily comply with our hypotheses and generally reduce the level of waveform similarity. In contrast, smaller windows create instability in the slowness vector estimates. The analysis window was shifted along the seismogram, sliding 5 ms (1 sample) each step. We started with a window centered at 60 samples before the P wave arrival, and analyzed 61 consecutive windows. *Almendros et al.* [2004] estimated the relative apparent slowness vectors using the window with the minimum misfit. We used a weighted average of the results corresponding to windows around the P wave arrival with low residuals (below 5 ms). This approach improves the stability of the final estimate.

[34] In this way, we calculated relative apparent slowness vectors for the P wave arrivals of 124 of the 150 earthquakes contained in 14 of the 17 clusters selected. The remaining earthquakes (including three full clusters) did not produce residuals below 5 ms, and were ruled out. The estimates of the absolute apparent slowness vectors were obtained by adding the absolute apparent slowness vector of the corresponding master event.

7.3. Precise Spatial Locations

[35] The application of the methodology described above provides estimates of the apparent slowness vectors for the earthquakes of each cluster. These estimates are highly accurate in a relative sense; that is, the differences between the vectors are precisely known thanks to the RelSE technique. Their absolute values, however, are based on the initial estimates of the apparent slowness vectors of the master event performed with the ZLCC method.

[36] The apparent slowness vectors provide the apparent slownesses and propagation azimuths of the P waves. We need the S-P delays to enable us to apply a ray-tracing procedure and locate the hypocenters. In order to measure the S-P delays with higher accuracy, we again used a rela-

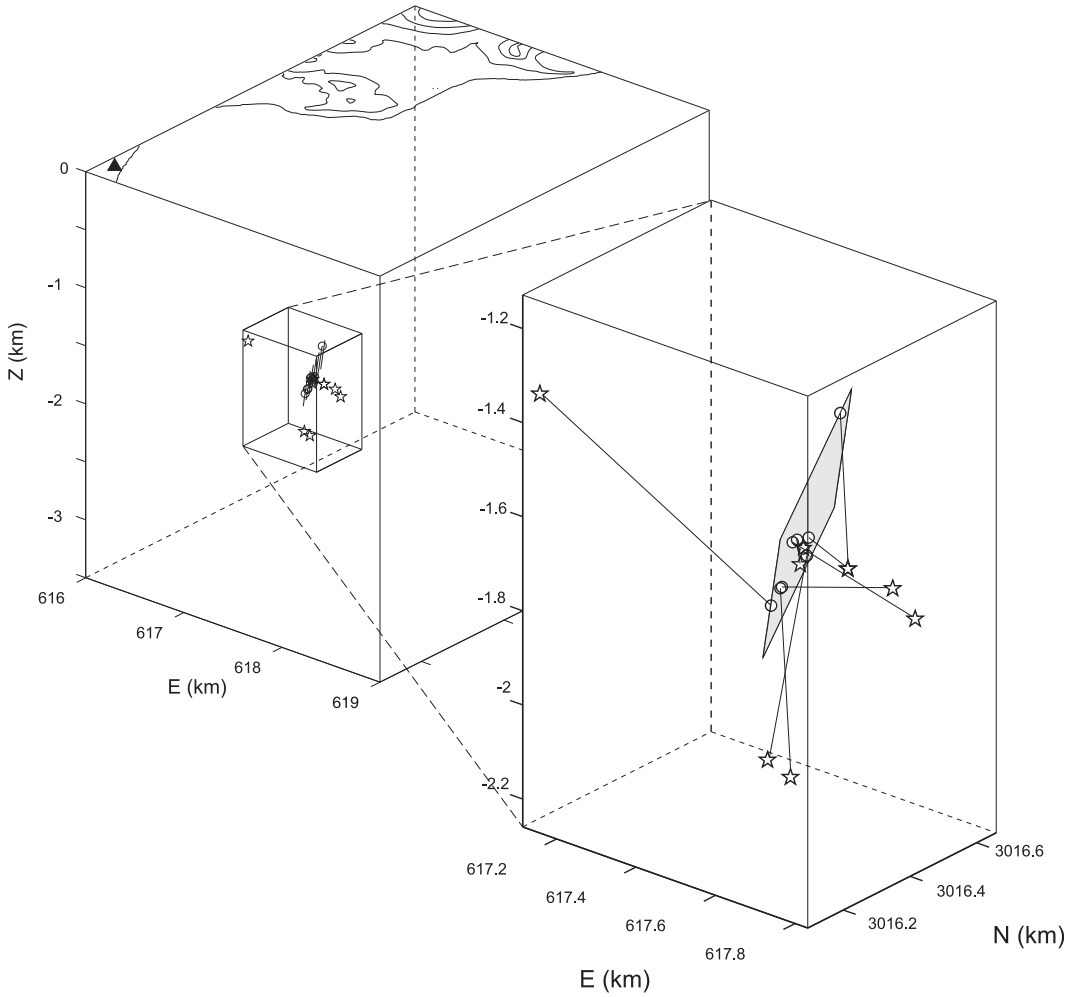

Figure 8. Comparison of source locations obtained using standard ZLCC (stars) and RelSE slowness vector estimates (open circles) for cluster 5. Shown is a 3-D view of the Fumarole Bay area, including the position of the seismic array (solid triangle). In the detailed view of the source region, a black line joins the source locations obtained using the ZLCC and RelSE methods. For the RelSE solutions, we show the best fit plane in gray.

tive approach. We performed spline interpolations of the cross-correlation functions between the earthquakes and their corresponding master event for the P and S wave arrivals. This technique makes use of the enhanced waveform similarity observed within the VT earthquake clusters, and reduces the uncertainty of the visual picking on the seismograms.

[37] The spatial locations of the hypocenters were obtained from the apparent slowness vectors and S-P delays using a ray-tracing procedure on a 1-D model, as described above. Figure 7 shows the results for the 14 clusters selected. We can see four epicentral areas. The closer area is just 1–2 km away from the array, and contains most of the clusters we analyzed (1, 3, 5, 11, 13, 18, 29, and 31). Another area is located opposite Punta Murature and contains three clusters (6, 21, and 25). The remaining areas contain just one cluster: number 14, located in the W side of the epicentral region; and number 4, located at about 3 km to the N. Most clusters fall within a narrow depth range of between 1.2 and 2.0 km. Only cluster 14 is deeper and lies between 2.8 and 3.2 km.

7.4. Plane Fitting

[38] The accuracy of the relative locations enabled us to address the shape of the hypocenter distributions. For most of the clusters, the distributions had a predominantly planar component. They were somewhat elongated in depth, due to the larger sizes of the uncertainty regions, but in general they defined a plane. We used a least squares approach to calculate the parameters of the plane that best fitted the distribution of the hypocenters. The quality of the fit was controlled by three parameters: (1) the misfit R, defined as the average misfit of the hypocenters to the best fit plane; (2) Q, the ratio of the average misfit R and the average distance of the projections of the hypocenters on the plane to the center of the distribution; and (3) the planarity P, defined as $1 - \lambda_3/\lambda_2$, where $\lambda_2 > \lambda_3$ are the two smallest eigenvalues of the covariance matrix of the hypocenter distribution. Both Q and P are measures of the oblateness of the hypocenter distribution. An optimal fit should have low R, low Q, and high P. Figure 8 shows an example of the results obtained with this procedure for a sample cluster.

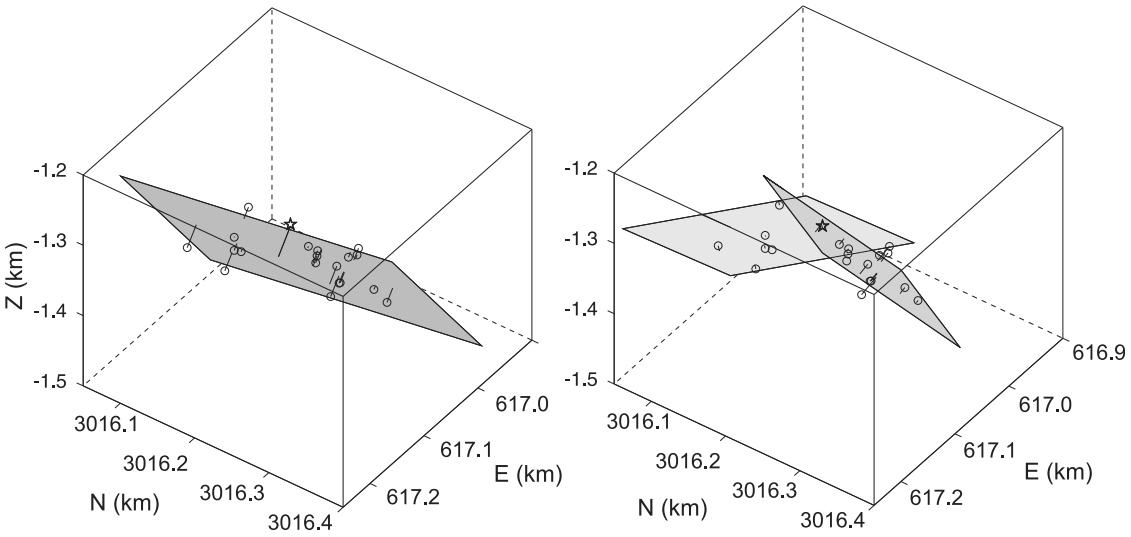

Figure 9. (left) Best fit plane for cluster 3, using all the earthquakes. (right) Best fit planes for clusters 3a and 3b, using two spatially distinct subgroups of earthquakes.

[39] We were able to fit planes to the 14 selected clusters. In two cases (clusters 3 and 6) the method discriminated two spatially distinct subgroups of hypocenters within the cluster. The quality of the plane fit including all members of the cluster was very low. However, the plane fits to these subgroups provided better results (Figure 9). In fact, there were slight variations in the waveforms that were indiscernible to the cluster detection algorithm. We therefore decided to subdivide these clusters (3a, 3b; 6a, 6b) and obtained a total of 16 planes.

[40] Table 1 shows the results of the fit for all the clusters. Table 1 contains (1) the cluster ID, (2) the number of earthquakes in each cluster and the number of earthquakes used for the fit, (3) measures of the quality of the fit (misfit, Q, and planarity), and (4) the plane orientation (strike and dip) and the angle θ defined as the angle between the plane strike and the line joining the array center and the master event hypocenter. We defined the strike between 0 and 360°, and measured it in such a way that the dip angle was measured to the right and did not exceed 90°.

[41] Misfits range from 3 to 18 m. The distances on the plane between hypocenter projections are in the order of hundreds of meters, which gives us some idea of the planar shapes of the distributions. This can be also seen from the Q parameter and the planarity. Q is always small, under 17%. Most distributions have a high planarity above 0.75. This threshold is similar to the limit used in other works to define the significant range of planarity [e.g., *Shearer et al.*, 2003].

[42] Strike angles range from 119 to 322°N, although most planes are oriented NW–SE. Dip angles vary between 41 and 86°. Most of them are large, which suggests the presence of subvertical planes. Figure 10 shows histograms of the strike and dip angles from Table 1, as well as Q and P. We also show horizontal projections of the strikes and a stereographic representation of the 16 planes. Figure 11 shows the locations and orientations of the planes found. Warm colors indicate high-quality fits (Animation S1).[1] The orientations of the planes with respect to the array (the angles θ) range between 17 and 130°. Most fits are characterized by θ values different from 90°, which reveals that they are not planes perpendicular to the line array hypocenter.

8. Discussion

8.1. Validity of the Methodology

[43] Relative location methods are among the most commonly used seismological tools for investigating the precise spatial distribution of the earthquake hypocenters. This technique is often used when a sufficient number of earthquakes with similar waveforms have been recorded by a seismic network. In this case we are able to find clusters of earthquakes with similar source locations and mechanisms.

Table 1. Summary of Multiplet Cluster Geometry for the Plane Fitting Procedure for the 16 Selected Clusters[a]

Cluster ID	Number of Earthquakes	Earthquakes Used in Fit	R (m)	Q (%)	P	Strike (°N)	Dip (deg)	θ (deg)
1	7	6	15.0	10.3	0.47	155	49	107
3a	9	7	3.6	6.4	0.98	129	59	65
3b	13	13	11.1	17.2	0.81	193	62	130
4	7	6	7.9	5.1	0.93	323	85	113
5	11	9	9.7	14.5	0.92	143	56	76
6a	12	12	13.5	13.5	0.75	233	86	17
6b	9	9	3.07	5.3	0.99	307	83	91
11	6	5	3.2	1.1	0.99	301	81	82
13	6	5	9.2	7.0	0.88	126	86	59
14	5	5	12.2	9.0	0.96	140	41	131
18	9	5	2.4	1.5	0.94	212	70	140
21	10	10	4.5	3.4	0.98	132	81	94
25	7	7	3.2	3.3	0.99	313	84	94
26	6	5	3.4	3.7	0.96	155	68	88
29	14	14	18.2	14.3	0.91	119	60	56
31	5	4	5.8	5.3	0.89	138	82	69

[a]Columns give from left to right the cluster ID; the number of events contained in each cluster; the number of events for the plane used in the fit; misfit R of the relative locations to the best fitting plane; Q; planarity P; and strike, dip, and θ angles.

[1]Auxiliary materials are available in the HTML. doi:10.1029/2009JB006865.

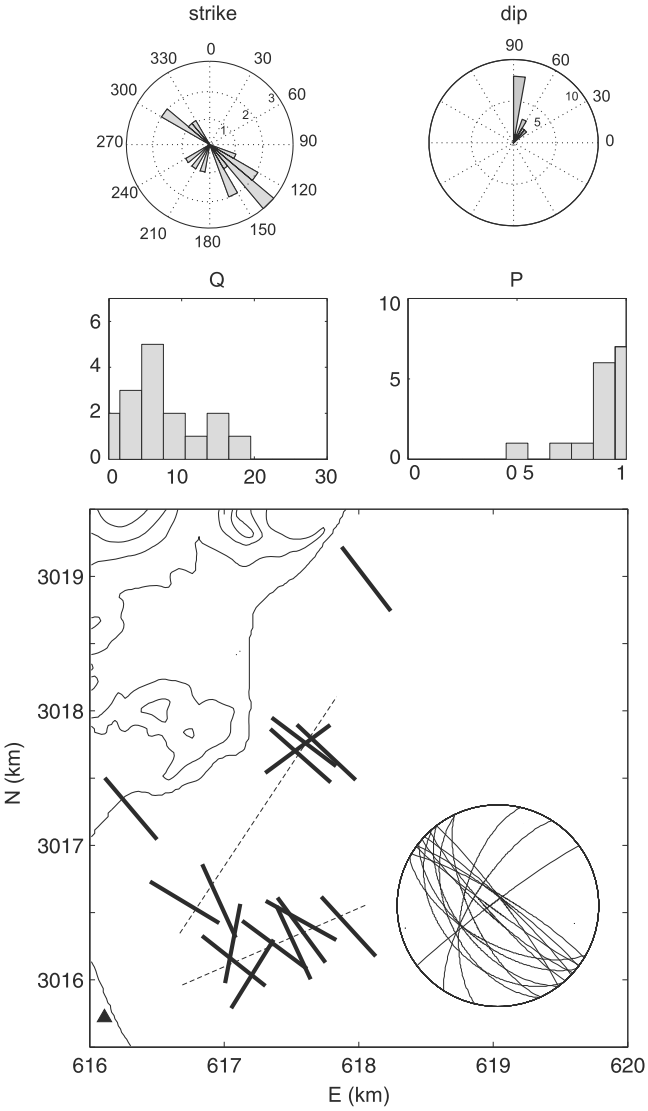

Figure 10. (top and middle) Histograms of strikes, dip angles, Q, and planarities of the best fitting planes from Table 1. (bottom) Representation of the strikes of the fracture planes at the corresponding master event epicenters. The alignments of the epicenters obtained from the initial relocations of the series (see Figure 6) are shown as dashed lines. The inset shows a stereographic representation of the fracture planes.

[44] Seismic arrays are often used in volcanic regions. To obtain precise locations from array data, we start with the relative apparent slowness vector estimated method [*Almendros et al.*, 2004]. This method allows the precise determination of the differences between the apparent slowness vectors among the members of a cluster. Using these differences, we have developed and applied a methodology to define fracture planes. It is based on ray tracing on a 1-D model and the fit of the distribution of hypocenters to a plane. The results provide information on the geometry of the faults implied in the earthquake generation, although they do not address the dynamics of the rupture process.

[45] The seismic series we analyze took place at Deception Island during the austral summer of 1998–1999. VT waveforms were repetitive, which allowed us to search for earthquake clusters. The correlation thresholds used to evaluate the similarity of P and S waveforms were high (~0.9). With these restrictive thresholds we ensured that the earthquakes within a cluster were very similar, so guaranteeing the efficiency of the RelSE method [*Almendros et al.*, 2004]. However, we obtained relatively few events per cluster. Only 17 of the 48 clusters contained 5 or more earthquakes.

[46] We obtained fracture planes for 14 clusters. For 12 of these clusters we obtained just one rupture plane, while the other 2 provided two planes each. This result emphasizes the sensitivity of the method, which was able to separate two subgroups of hypocenters spatially within the same cluster. There are small variations in the waveforms (see for example the amplitude of the S wave given by *Almendros et al.* [2004, Figure 10]). These variations have virtually no impact on the cluster selection procedure, but produce different estimates of the relative apparent slowness vectors. This feature has also been observed in the case of relative location methods that use seismic network data [e.g., *Carmona et al.*, 2009].

[47] The quality of the results is related to different factors that may affect the methodology. The most important factors are related to the quality of the spatial location of the hypocenters. These include (1) the effect of the velocity model used to represent the medium, (2) the uncertainty in the estimate of the apparent slowness vector of the master event, and (3) the choice of a master event within each cluster.

[48] We began by testing the effect of the velocity model in the geometry of the fracture planes calculated. We generated 100 velocity models using random variations of the three parameters A,B,C that define the model. These values were obtained from normal distributions centered at the values of the parameters in the original model. The standard deviations were fixed to 25% of the central values. For each of these models we calculated the precise relative locations and the best fit plane.

[49] Although the original velocity model changes significantly during the above process (Figure 12), the geometry of the best fit plane is relatively stable. The parameters that define the plane remain similar to the parameters obtained in the original model. For example, Figure 12 shows the distributions of strike, dip, Q, and P obtained for cluster 5. The dispersion of the results is larger for the dip angle than for the strike. The depth of the hypocenters is more sensitive to the velocity variations in the model.

[50] We also tested the effect of the choice of Vp/Vs ratio. Again, we generated 100 velocity models with random variations of the Vp/Vs ratio. We used a normal distribution with mean of 1.73 and standard deviation of 10%. Although the absolute locations are slightly different, the results suggest that the Vp/Vs ratio has a very limited effect on the characteristics of the best fit planes (Figure 13).

[51] The second factor that affects the results is the estimate of the absolute apparent slowness vector of the master event. We generated random distributions of azimuth and apparent slowness of the master event. We used normal distributions centered at the azimuth and apparent slowness obtained using the ZLCC method. The standard deviations were obtained from the size of the 90% uncertainty area on

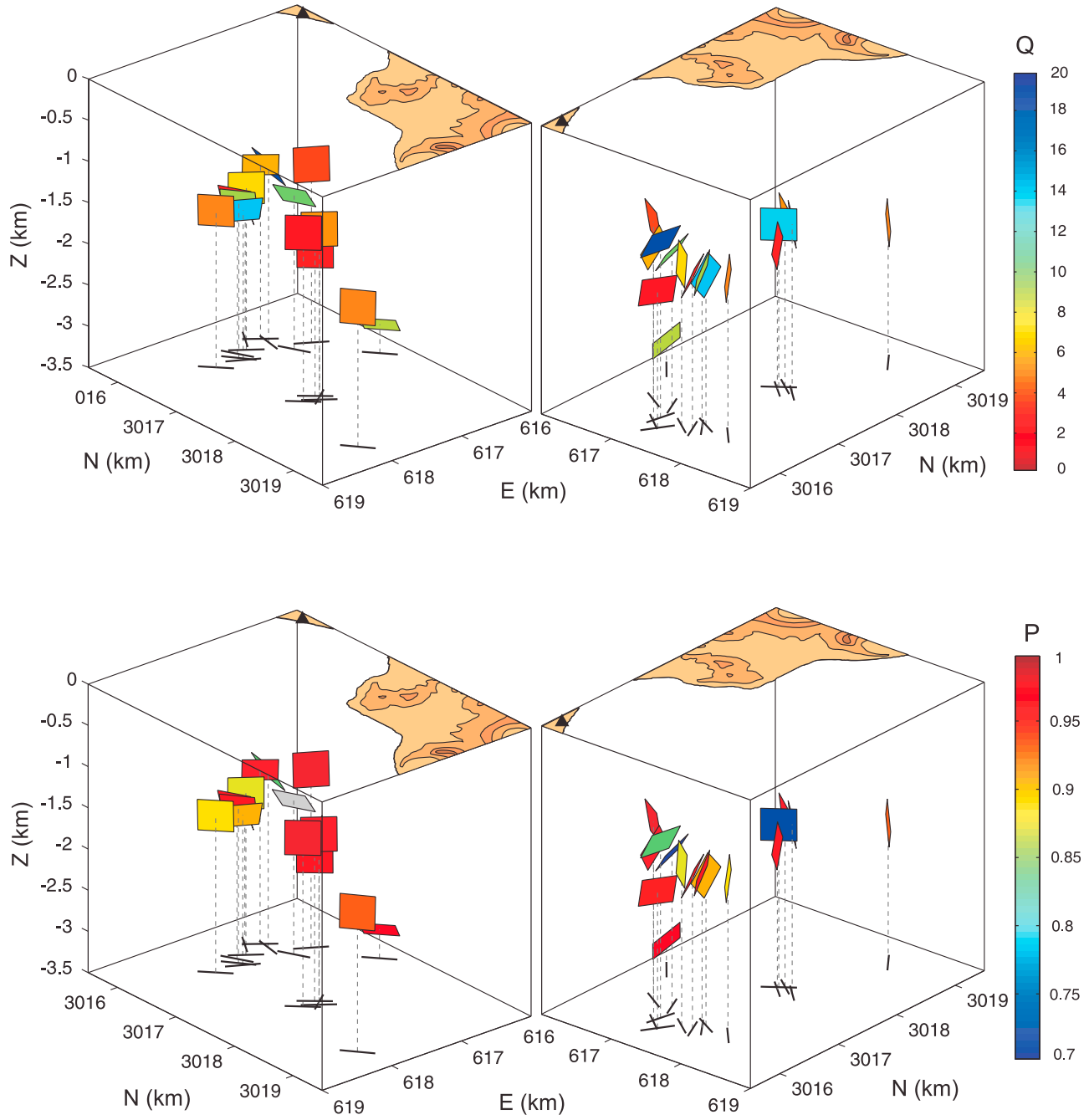

Figure 11. Three-dimensional view of the best fitting planes obtained for the 16 clusters. Planes are shown at the corresponding master events locations from two different perspectives. The color scale represents the quality of the fit, in terms of (top) Q and (bottom) planarity. Warm colors indicate high-quality fits. The black lines are projections of the plane strikes. The array position is shown by a triangle. Topography is represented with a contour interval of 50 m.

the apparent slowness plane. Figure 14 shows a summary of the results.

[52] For variations in the azimuth of the master event, we found a marked stability in the strike and dip of the planes. This result was anticipated, since a change in the propagation azimuth implies a rotation of the hypocenters around the array, without any change in their relative positions. In a laterally homogeneous model, a rotation does not modify the angle θ between the strike of the best fit plane and the line joining the array center and the master hypocenter. The dip angle is independent of the azimuth, while the variations in strike are related to the variations introduced in the absolute azimuth of the master event.

[53] The variations in the apparent slowness of the master event also produced a high stability in the strikes, but there was more dispersion in the dip angles. A change in the absolute slowness yielded a change in the depth of the hypocenters and therefore a change in the inclination of the

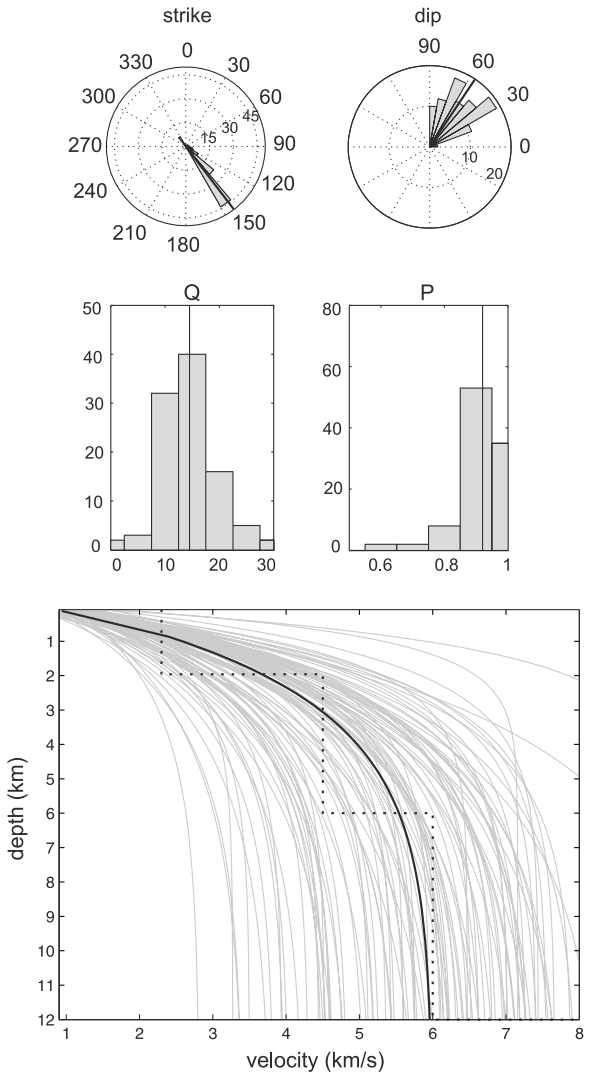

Figure 12. Results of the test on the effect of the velocity model for cluster 5. (top and middle) Histograms of strikes, dip angles, Q, and planarities for random variations of the velocity model parameters. The black lines indicate the values obtained using our smoothed velocity model. (bottom) Original velocity model (black dotted line), smoothed velocity model (black solid line), and random velocity models used in the test (gray lines).

best fit plane. However, the strike was stable, which suggests that the estimate is robust.

[54] Both for variations of the azimuth and the apparent slowness of the master event, the values Q and P defining the quality of the fits are similar to those obtained in the fit of the original hypocenter distributions. These results indicate that the hypocenter distributions maintain planar structures for variations of the absolute apparent slowness vectors of the master events within their uncertainties.

[55] The third factor is the selection of a master event. *Almendros et al.* [2004] demonstrated that the relative apparent slowness vectors are independent of the choice of master event. However, the absolute apparent slowness vectors of the cluster members (obtained by adding the absolute apparent slowness vector of the corresponding master event) do depend on the choice of master event. In our case, the differences are not significant, since the estimates of apparent slownesses and azimuths obtained with the ZLCC method for each cluster range within relatively narrow margins. For example, for cluster 5 the maximum difference of azimuths among cluster members is about 10°, and the maximum difference of slowness is about 0.05 s/km. These values are the same size as the 90% uncertainty regions associated with the ZLCC estimates. Therefore, the selection of a different master event is equivalent to an error in the estimate of the apparent slowness vector of the master event. And we have already tested that the solutions are stable.

[56] In any case, it is important to select events with a good signal-to-noise ratio and a large maximum average correlation with the ZLCC method. The absolute location of the master event should be as accurate as possible, since we

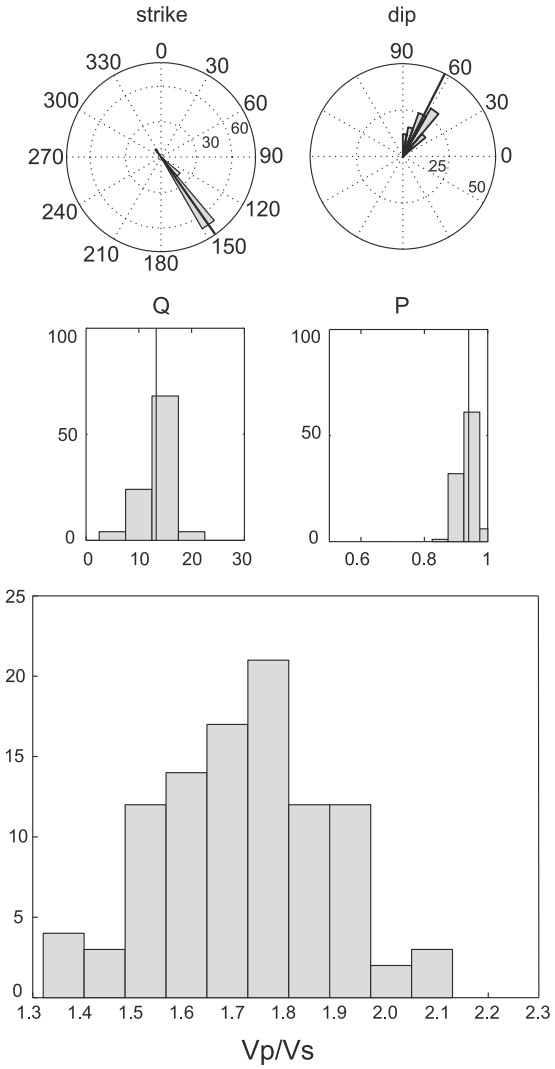

Figure 13. Results of the test on the effect of the Vp/Vs ratio for cluster 5. (top and middle) Histograms of strikes, dip angles, Q, and planarities for random variations of the Vp/Vs ratio. The black lines indicate the values obtained using a Vp/Vs ratio of 1.73. (bottom) Histogram of the random Vp/Vs ratios used in the test.

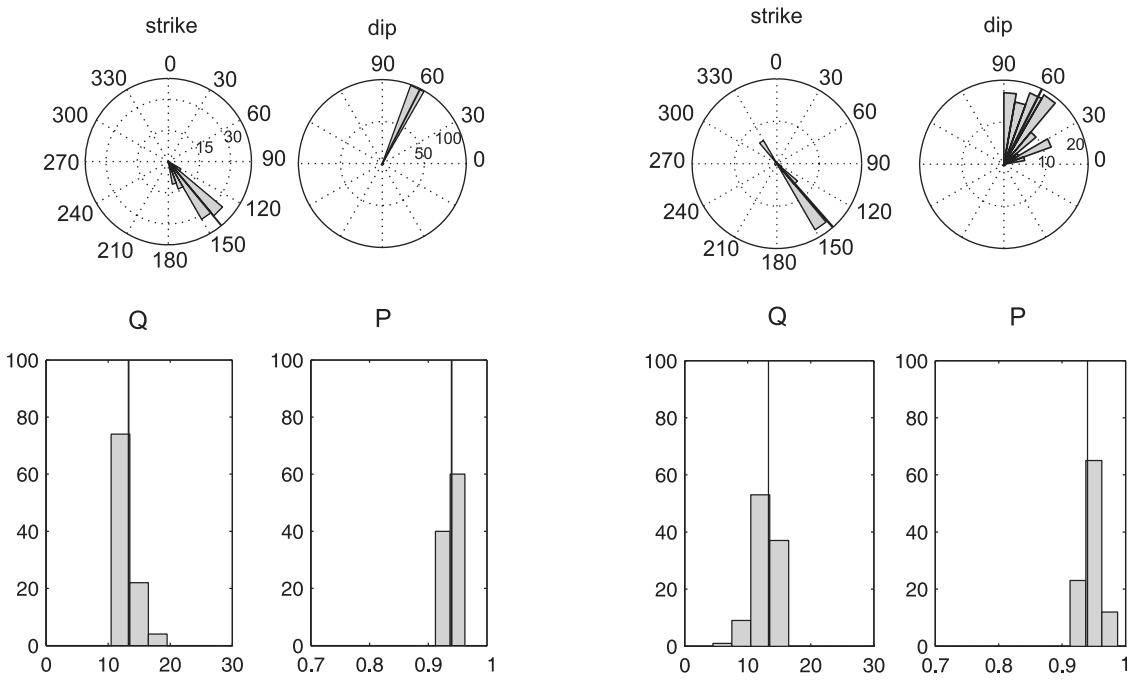

Figure 14. Results of the test on the effect of the estimate of the apparent slowness vector of the master event on the plane geometry for cluster 5. (left) Histograms of strikes, dip angles, Q, and planarities of the best fit plane for random variations of the azimuth of the master event. (right) Histograms of strikes, dip angles, Q, and planarities of the best fit plane for random variations of the apparent slowness of the master event. The black lines indicate the values obtained using the apparent slowness and propagation azimuth of the master event estimated with the ZLCC method.

use it to position the other cluster members and to interpret the relative positions of the different clusters selected.

[57] We calculate the θ angle to characterize the relative position of the best fit plane and the array. We observe that for some clusters the S-P delays are practically the same for all the cluster members. In this case, all earthquakes would be at the same distance from the array. The fit would yield a plane with $\theta = 90°$ regardless of the estimates of the relative apparent slowness vectors. In our results, there were five planes with θ angles between 80 and 100° that could be in that situation. But the fact that we found other orientations indicates that the relative locations obtained from the RelSE method are crucial to the definition of a plane. In any case, we performed a test to investigate the geometry and quality of a fit based on random locations. We generated hypocenter distributions based on random values of the relative apparent slowness vectors and S-P measures. We used normal distributions centered in the values of the master event, with standard deviations given by the maximum dispersion of the parameters within each cluster. Figure 15 shows the results obtained for two clusters. The cluster with a θ angle other than 90° does not show any agreement with the parameters derived from the random test. The cluster with a θ angle near 90° does show a strike perpendicular to the back azimuth of the master. However, the fits of the random hypocenters do not have the quality achieved by the real data. They show lower P and higher Q compared with our results for the cluster. Again, this demonstrates that a precise estimate of the relative apparent slowness vectors is essential for the characterization of the fracture planes.

8.2. Interpretation of the Results

[58] The final results of our fracture characterization procedure show that the majority of the planes have strikes in the 120–140°N direction (NW–SE). These trends coincide with some of the major fault systems in the island described by other authors. For example, *Rey et al.* [1995] presented three fault systems: 160–170°N right-lateral strike-slip faults, 45–60°N normal faults and 115–120°N normal faults in the SW of the island. *Martí et al.* [1996] also describes three fault systems that cross the island NE–SW, NW–SE and N–S. The most relevant seems to be the NE–SW system [*Smellie*, 1988]. *González-Casado et al.* [1999] also set out three main systems of microfractures: NE–SW, E–W and NW–SE, with dips greater than 60° and related to the NW–SE extension of the Bransfield Strait. These same authors state that the faults with NW–SE direction are transfer faults from the NE–SW systems. *Smellie and López-Martínez* [2000] made a geomorphological map of Deception Island in which normal NW–SE faults appear in our study area. *Paredes et al.* [2006] presented a morphoalignment map that showed the directions of the fractures in the island. They summarized all the work to date and combined it with a morphometric analysis of the digital elevation model, to create a synthesis map of the traces of faults. The preferred directions were NE–SW, N–S and NNW–SSE.

[59] The predominant NW–SE direction found in our results coincides with some alignments reported by these authors. The directions of the other strikes are between 190 and 240°N, which also coincide with alignments described

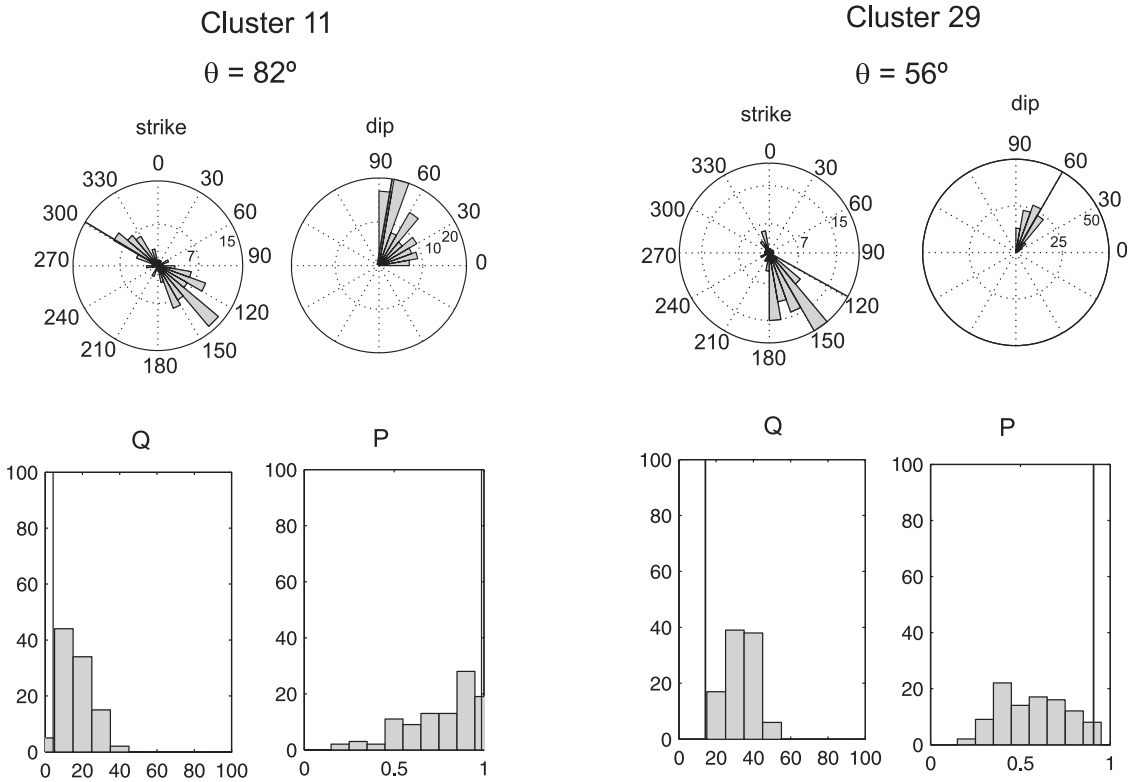

Figure 15. Results of the test on the reliability of those plane solutions that are perpendicular to the array hypocenter direction. Shown are histograms of strikes, dip angles, Q, and planarities for random variations of relative apparent slowness vectors and S-P times within limits obtained from clusters (left) 11 and (right) 29. The black lines indicate the values corresponding to our best fit plane.

previously (NS and NE–SW). The dips of the planes, mostly subvertical, are consistent with the characteristics of the fault systems that are expected in an extensional area [*González-Casado et al.*, 1999].

[60] Both the distribution of the epicenters found by *Ibáñez et al.* [2003b] and our initial relocations shown in Figure 6 show two preferred alignments in directions NE–SW and ENE–WSW. These directions do not match the directions obtained from the geometry of the rupture planes of the series (Figure 10). The consequence is that the interpretation of epicentral maps in terms of fracture alignments can be severely biased, since we have no information about the real directions of rupture. The local tectonic regime can only be addressed using information on the source mechanisms, or at least with the definition of rupture planes using precise relative locations.

[61] We found 16 fracture planes in the Fumarole Bay area. We were unable to investigate other areas of the island, since all the selected families occur in this area. However, *Ibáñez et al.* [2003b] showed that the accumulation of epicenters in the vicinity of the array is an apparent effect due to the low magnitude of the events and the high attenuation of the medium under Port Foster [*Vila et al.*, 1995; *Martínez-Arévalo et al.*, 2003]. It is likely that there are distributions of similar fractures in the area N of Port Foster, where some of the more distant earthquakes in the series are located (Figure 2).

[62] To some extent, one could interpret that the directions obtained from the planes are distributed parallel and perpendicular to the edge of the caldera in the Fumaroles area. This could suggest the presence of ring fracture systems related to the formation of a caldera collapse. However, the stability of the orientations of the planes (Figures 10 and 11) suggests a close relationship with the regional tectonics, as has been suggested by other authors [*Martí et al.*, 1996; *Rey et al.*, 1995; *González-Casado et al.*, 1999].

[63] The ruptures of the planes identified in our analyses could be a consequence of regional tectonics, volcanic activity, or a mixture of both. *Ibáñez et al.* [2003b] rule out the first two hypotheses, since they do not fit their results. These authors suggest that the most likely explanation for the origin of the series is the development of a magmatic intrusion that produced a change in the local stress field but did not reach the surface.

[64] Studies of deformation of Deception Island suggest that there are two main directions of deformation related to the regional tectonics and volcanic activity of Deception Island [*Fernández Ros et al.*, 2007]. After the 1999 crisis there was a change in the movement of the island. It changed from an extension and elevation of the entire island to a compressive process of subsidence in the N and NW areas [*Berrocoso et al.*, 2008]. The work of *Caselli et al.* [2004] on the geochemistry of gases in the Fumarole Bay area after the 1999 crisis shows an increased SO_2 flux. This increase appears to be related to the intrusion of dykes into surface layers. This resulted in the emergence of native sulfur deposits and iron sulfides in thin layers in the fumarolic system. These works highlight the relationship between

a volcanic reactivation and the emergence of swarms of VT earthquakes in 1999.

[65] What seems clear is that a reactivation of the magma chamber of Deception Island would trigger an imbalance in the area. This may be the cause of the 1999 series of VT earthquakes. Seismic tomography has imaged a shallow magma chamber at Deception Island volcano [*Zandomeneghi et al.*, 2009; *Ben-Zvi et al.*, 2009]. This chamber is situated at a depth of about 2–4 km under the inner bay of Deception, slightly shifted toward the W, elongated NW–SE direction. Deformation studies have situated the center of the superficial deformation produced after the 1999 crisis in the bay off Obsidianas Beach [*Berrocoso et al.*, 2008]. Other studies had already suggested a possible resurgence of the Port Foster floor [*Cooper et al.*, 1998] after the 1992 series. This area coincides with the position of the magma chamber established by seismic tomography studies. This fact indicates that the activation of the chamber was the origin of the series.

[66] The fault planes and their locations might be consistent with a trapdoor model. These near-vertical faults would form the opening of a trapdoor, with the hinge located along the E or NE coast of Port Foster. There is evidence for faulting along the NW and SW boundaries of the inferred magma body [*Maestro et al.*, 2007; *Barclay et al.*, 2009] and the fault strikes in Figure 10 might indicate high-angle faulting along the edge of an inflating magma chamber. However, the trapdoor hypothesis requires the absence of active fractures in the E or NE sector of Port Foster. Given the low magnitude of the earthquakes, we cannot exclude the (undetected) presence of fracture planes in this area.

[67] Seismic tomography also indicates low velocities to a depth of 2 km in the Fumarole Bay area, suggesting a highly fractured medium, which supports our results. The fractures involved in the series are situated in or within the limits of the magma chamber. This should be an area of high-temperature rocks, which should show a somewhat ductile behavior, thus preventing the occurrence of VT earthquakes. However, VT earthquakes are commonly found within low-velocity bodies in volcanoes [*Dawson et al.*, 1999; *Waite and Moran*, 2009], which indicates that the medium is rigid enough to produce earthquakes. The vicinity of the magma chamber could explain why we detected VT activity and hybrid events (i.e., presence of fluids) in the same place. The presence of magmatic fluids would increase the pore pressure, resulting in an increase of the normal stress acting on the fault plane. This facilitates the rupture processes responsible of the VT earthquakes. In any case, the faults should be consistent with the framework of the regional tectonics affecting the volcanic evolution of Deception Island.

9. Conclusions

[68] We have developed a method to investigate the geometry of the fractures involved in a series of VT earthquakes recorded by a seismic array. The method exploits the similarity of the waveforms that appear in the seismic series to perform accurate estimates of the apparent slowness vector and the difference of S-P times. With these estimates, we obtain precise relative locations that indicate the orientation of the fracture.

[69] Although the method for characterization of fracture planes through relative locations using seismic networks is widespread, this is the first time that results of equivalent quality are achieved using data recorded by a seismic array. The sensitivity of the method is very high, to the extent that it is able to discern small differences in the waveforms within a family of earthquakes and separate the events spatially. In two cases this has enabled us to identify two fracture planes within the same family.

[70] To check the stability of our method for characterization of fractures we have carried out a series of tests. We have investigated the effect of the selection of the velocity model that is used to locate the earthquakes, the uncertainty in the estimation of the apparent slowness vector of the master event, and the choice of master event among the members of each cluster. The results show that the estimate of the strike is very robust in all cases, while the dip is more influenced by the characteristics of the model and the value of the apparent slowness of the master.

[71] The fracture planes obtained in this work reveal the presence of active faults in the Fumarole Bay area. The strikes clearly show that most of the planes have a NW–SE trend while a few run NE–SW. These strikes are coincident with fracturing directions listed in other works about the island. The dips are mostly subvertical, which is consistent with the existence of normal faults related to the extension of the Bransfield Basin. The geometry and position of these planes show that the 1999 series was influenced by regional tectonics, although the origin of the destabilization of the system is related to the reactivation of a shallow magma chamber.

[72] We have created an analysis tool that can be easily applied in those volcanoes where arrays are used. The method provides the basis to determine rupture planes of the VT events and obtain information on the local tectonic regime using only a seismic array. The simplicity of array logistics, easy maintenance, etc, compared to the deployment of a seismic network, and the equivalence of the quality of the results, means that the methodology should have successful applications in volcanic areas.

[73] **Acknowledgments.** We thank an anonymous reviewer for useful comments and suggestions. This work has been partly supported by projects ANT-1111, TOMODEC, POL2006-08663, and CGL2008-01660 of the Spanish Ministry of Science and Innovation. We thank all the participants in the 1998–1999 seismic survey, especially F. Calexico. We are also grateful to G. Saccorotti, M. Abril, and L. Buontempo for their support.

References

Almendros, J., J. M. Ibáñez, G. Alguacil, E. Del Pezzo, and R. Ortiz (1997), Array tracking of the volcanic tremor source at Deception Island, Antarctica, *Geophys. Res. Lett.*, *24*, 3069–3072, doi:10.1029/97GL03096.

Almendros, J., J. M. Ibáñez, G. Alguacil, and E. Del Pezzo (1999), Array analysis using circular wavefront geometry: An application to locate the nearby seismo-volcanic source, *Geophys. J. Int.*, *136*, 159–170, doi:10.1046/j.1365-246X.1999.00699.x.

Almendros, J., J. M. Ibáñez, G. Alguacil, J. Morales, E. Del Pezzo, M. La Rocca, R. Ortiz, V. Araña, and M. J. Blanco (2000), A double seismic antenna experiment at teide Volcano: Existence of local seismicity and lack of evidences of volcanic tremor, *J. Volcanol. Geotherm. Res.*, *103*, 439–462, doi:10.1016/S0377-0273(00)00236-5.

Almendros, J., B. Chouet, and P. Dawson (2001a), Spatial extent of a hydrothermal system at Kilauea Volcano, Hawaii, determined from array analyses of shallow long-period seismicity: 1. Method, *J. Geophys. Res.*, *106*(B7), 13,565–13,580, doi:10.1029/2001JB000310.

Almendros, J., B. Chouet, and P. Dawson (2001b), Spatial extent of a hydrothermal system at Kilauea Volcano, Hawaii, determined from array analyses of shallow long-period seismicity: 2. Results, *J. Geophys. Res.*, *106*(B7), 13,581–13,597, doi:10.1029/2001JB000309.

Almendros, J., E. Carmona, and J. M. Ibáñez (2004), Precise determination of the relative wave propagation parameters of similar events using a small aperture seismic array, *J. Geophys. Res.*, *109*, B11308, doi:10.1029/2003JB002930.

Almendros, J., J. M. Ibáñez, E. Carmona, and D. Zandomeneghi (2007), Array analyses of volcanic earthquakes and tremor recorded at Las Cañadas caldera (Tenerife Island, Spain) during the 2004 seismic activation of Teide volcano, *J. Volcanol. Geotherm. Res.*, *160*, 285–299, doi:10.1016/j.jvolgeores.2006.10.002.

Alparone, S., and S. Gambino (2003), High precision locations of multiplets on south–eastern flank of Mt. Etna (Italy), reconstruction of fault plane geometry, *Phys. Earth Planet. Inter.*, *135*, 281–289, doi:10.1016/S0031-9201(03)00048-7.

Aster, R. C., and J. Scott (1993), Comprehensive characterization of waveform similarity in microearthquake data sets, *Bull. Seismol. Soc. Am.*, *83*, 1307–1314.

Baker, P. E., I. McReath, M. R. Harvey, M. J. Roobol, and T. G. Davis (1975), The Geology of the South Shetland Islands: V. Volcanic evolution of Deception Island, *Br. Antarct. Serv. Sci. Rep.*, *78*, 1–81.

Baraldo, A., and C. A. Rinaldi (2000), Stratigraphy and structure of Deception Island, south Shetland Island, Antarctica, *J. South Am. Earth Sci.*, *13*, 785–796, doi:10.1016/S0895-9811(00)00060-2.

Barclay, A. H., W. S. D. Wilcock, and J. M. Ibáñez (2009), Bathymetric constraints on the tectonic and volcanic evolution of Deception Island Volcano, South Shetland Islands, *Antarct. Sci.*, *21*(2), 153–167, doi:10.1017/S0954102008001673.

Battaglia, J., C. H. Thurber, J. Got, C. A. Rowe, and R. A. White (2004), Precise relocation of earthquakes following the 15 June 1991 eruption of Mount Pinatubo (Philippines), *J. Geophys. Res.*, *109*, B07302, doi:10.1029/2003JB002959.

Battaglia, J., K. Aki, and V. Ferrazzini (2005), Location of tremor sources and estimation of lava using tremor source amplitude on the Piton de la Fournaise volcano: 1. Location of tremor sources, *J. Volcanol. Geotherm. Res.*, *147*, 268–290, doi:10.1016/j.jvolgeores.2005.04.005.

Ben-Zvi, T., W. S. D. Wilcock, A. Barclay, D. Zandomeneghi, J. M. Ibáñez, and J. Almendros (2009), The P wave velocity structure of Deception Island, Antarctica, from two-dimensional seismic tomography, *J. Volcanol. Geotherm. Res.*, *180*, 67–80, doi:10.1016/j.jvolgeores.2008.11.020.

Berrocoso, M., et al. (2008), Geodetic research on Deception Island and its environment (South Shetland Islands, Bransfield Sea and Antarctic Peninsula) during Spanish Antarctic campaigns 1987–2007, in *Geodetic and Geophysical Observations in Antarctica*, edited by A. Capra and R. Dietrich, pp. 97–123, doi:10.1007/978-3-540-74882-3_6, Springer, Berlin.

Brancato, A., and S. Gresta (2003), High precision relocation of microearthquakes at Mt. Etna (1991–1993 eruption onset), a tool for better understanding the volcano seismicity, *J. Volcanol. Geotherm. Res.*, *124*, 219–239, doi:10.1016/S0377-0273(03)00071-4.

Carmona, E., F. Martini, J. M. Ibáñez, and C. J. Bean (2007), Multiplets and detection of seismic velocity changes during the 1998–99 seismic series at Deception Island Volcano, Antarctica, *Eos Trans. AGU*, *88*(52), Fall Meet. Suppl., Abstract V53C-1415.

Carmona, E., D. Stich, G. Saccorotti, and J. M. Ibáñez (2009), Multiplet focal mechanisms from polarities and relative locations: The Iznajar swarm in Southern Spain, *Bull. Seismol. Soc. Am. 99*, 3421–3429, doi:10.1785/0120090036.

Caselli, A. T., M. Santos-Alfonso, and M. R. Agusto (2004), Gases fumarólicos de la isla Decepción (Shetlands del Sur, Antártida): Variaciones químicas y depósitos vinculados a la crisis sísmica de 1999, *Asoc. Geol. Argent. Rev.*, *59*, 291–302.

Chouet, B. (1996), Long-period volcano seismicity: Its source and use in eruption monitoring, *Nature*, *380*, 309–316, doi:10.1038/380309a0.

Chouet, B., G. Saccorotti, M. Martini, P. Dawson, G. De Luca, G. Milana, and R. Scarpa (1997), Source and path effects in the wave fields of tremor and explosions at Stromboli Volcano, Italy, *J. Geophys. Res.*, *102*, 15,129–15,150, doi:10.1029/97JB00953.

Cooper, A. P. R., J. L. Smellie, and J. Maylin (1998), Evidence for shallowing and uplift from bathymetric records of Deception Island, Antarctica, *Antarct. Sci.*, *10*, 455–461, doi:10.1017/S0954102098000558.

Dawson, P. B., B. A. Chouet, P. B. Okubo, A. Villaseñor, and H. A. Benz (1999), Three-dimensional velocity structure of the Kilauea caldera, Hawaii, *Geophys. Res. Lett.*, *26*, 2805–2808, doi:10.1029/1999GL005379.

Deichmann, N., and M. García-Fernández (1992), Rupture geometry from high-precision relative hypocenter locations of microearthquake clusters, *Geophys. J. Int.*, *110*, 501–517, doi:10.1111/j.1365-246X.1992.tb02088.x.

Del Pezzo, E., M. La Rocca, and J. M. Ibanez (1997), Observations of high-frequency scattered waves using dense arrays at Teide volcano, *Bull. Seismol. Soc. Am.*, *87*, 1637–1647.

Fernández-Ibáñez, F., R. Pérez-López, J. J. Martínez-Díaz, C. Paredes, J. L. Giner-Robles, A. Caselli, and J. M. Ibáñez (2005), Costa Recta Beach, Deception Island, West Antarctica: A retreated scarp of a submarine fault?, *Antarct. Sci.*, *17*, 418–426, doi:10.1017/S0954102005002841.

Fernández Ros, A., M. Berrocoso, and M.E. Ramírez (2007), Volcanic deformation models for Deception Island (South Shetland Islands, Antarctica), *Rep. OF-2007–1047*, U.S. Geol. Surv., Reston, Va.

Frankel, A., S. Hough, P. Friberg, and R. Busby (1991), Observations of Loma Prieta aftershocks from a dense array in Sunnyvale, California, *Bull. Seismol. Soc. Am.*, *81*, 1900–1922.

Frémont, M. J., and S. D. Malone (1987), High precision relative locations of earthquakes at Mount St. Helens, Washington, *J. Geophys. Res.*, *92*, 10,223–10,236, doi:10.1029/JB092iB10p10223.

Geller, R. J., and C. S. Mueller (1980), Four similar earthquakes in Central California, *Geophys. Res. Lett.*, *7*, 821–824, doi:10.1029/GL007i010p00821.

Gillard, D., A. M. Rubin, and P. Okubo (1996), Highly concentrated seismicity caused by deformation of Kilauea's deep magma system, *Nature*, *384*, 343–346, doi:10.1038/384343a0.

González-Casado, J. M., J. López-Martínez, J. Giner, J. J. Durán, and P. Gumiel (1999), Análisis de la microfracturación en la isla Decepción, *Antártida occidental, Geogaceta*, *26*, 27–30.

González-Ferrán, O., and Y. Katsui (1970), Estudio integral del volcanismo cenozoico superior de las Islas Shetland del Sur, Antarctica, *Ser. Cient., Inst. Antart. Chileno*, *1*, 123–174.

Havskov, J., J. A. Peña, J. M. Ibáñez, L. Ottemöller, and C. Martínez-Arévalo (2003), Magnitude scales for very local earthquakes. Application for Deception Island volcano (Antarctica), *J. Volcanol. Geotherm. Res.*, *128*, 115–133, doi:10.1016/S0377-0273(03)00250-6.

Hensch, M., C. Riedel, J. Reinhardt, and T. Dahm (2008), Hypocenter migration of fluid-induced earthquake swarms in the Tjörnes Fracture Zone (North Iceland), *Tectonophysics*, *447*, 80–94, doi:10.1016/j.tecto.2006.07.015.

Ibáñez, J. M., J. Morales, G. Alguacil, J. Almendros, R. Ortiz, and E. Del Pezzo (1997), Intermediate-focus earthquakes under South Shetland Islands (Antarctica), *Geophys. Res. Lett.*, *24*(5), 531–534, doi:10.1029/97GL00314.

Ibáñez, J. M., E. Del Pezzo, J. Almendros, M. La Rocca, G. Alguacil, R. Ortiz, and A. García (2000), Seismovolcanic signals at Deception Island volcano, Antarctica: Wavefield analysis and source modeling, *J. Geophys. Res.*, *105*, 13,905–13,931, doi:10.1029/2000JB900013.

Ibáñez, J. M., J. Almendros, E. Carmona, C. Martínez-Arévalo, and M. Abril (2003a), The recent seismo-volcanic activity at Deception Island volcano, *Deep Sea Res., Part II*, 50, 1611–1629, doi:10.1016/S0967-0645(03)00082-1.

Ibáñez, J. M., E. Carmona, J. Almendros, G. Saccorotti, E. Del Pezzo, M. Abril, and R. Ortiz (2003b), The 1998–1999 seismic series at Deception Island volcano, Antarctica, *J. Volcanol. Geotherm. Res.*, *128*, 65–88, doi:10.1016/S0377-0273(03)00247-6.

Ibáñez, J. M., E. Del Pezzo, C. Bengoa, A. Caselli, G. Badi, and J. Almendros (2008), Volcanic tremor and local earthquakes at Copahue volcanic complex, southern Andes, Argentina, *J. Volcanol. Geotherm. Res.*, *174*, 284–294, doi:10.1016/j.jvolgeores.2008.02.005.

Jones, J. P., C. H. Thurber, and W. J. Lutter (2001), High-precision location of pre-eruption seismicity at Mount Pinatubo, Philippines, 30 May–3 June, 1991, *Phys. Earth Planet. Inter.*, *123*, 221–232, doi:10.1016/S0031-9201(00)00211-9.

La Rocca, M., S. Petrosino, G. Saccorotti, M. Simini, J. M. Ibáñez, J. Almendros, and E. Del Pezzo (2000), Location of the source and shallow velocity model deduced from the explosion quakes recorded by two seismic antennas at Stromboli Volcano, *Phys. Chem. Earth*, *25*, 731–735, doi:10.1016/S1464-1895(00)00113-7.

La Rocca, M., G. Saccorotti, E. Del Pezzo, and J. M. Ibáñez (2004), Probabilistic source location of explosion quakes at Stromboli volcano estimated with double array data, *J. Volcanol. Geotherm. Res.*, *131*, 123–142, doi:10.1016/S0377-0273(03)00321-4.

La Rocca, M., D. Galluzzo, S. Malone, W. McCausland, G. Saccorotti, and E. Del Pezzo (2008), Testing small-aperture array analysis on well-located earthquakes, and application to the location of deep tremor, *Bull. Seismol. Soc. Am.*, *98*(2), 620–635, doi:10.1785/0120060185.

Maestro, A., L. Somoza, J. Rey, J. Martínez-Frías, and J. López-Martínez (2007), Active tectonics, fault patterns, and stress field of Deception Island: A response to oblique convergence between the Pacific and Ant-

arctic plates, *J. South Am. Earth Sci.*, *23*, 256–268, doi:10.1016/j.jsames.2006.09.023.

Martí, J., J. Vila, and J. Rey (1996), Deception Island (Bransfield Strait, Antarctica): An example of volcanic caldera developed by extensional tectonics, *J. Geol. Soc.*, *110*, 253–265.

Martínez-Arévalo, C., F. Bianco, J. M. Ibáñez, and E. Del Pezzo (2003), Shallow seismic attenuation and shear-wave splitting in the short period range of Deception island volcano (Antarctica), *J. Volcanol. Geotherm. Res.*, *128*, 89–113, doi:10.1016/S0377-0273(03)00248-8.

Martínez-Arévalo, C., F. Mancilla, J. Almendros, J. L. Aznarte, and G. Alguacil (2009), Preliminary results of receiver function analyses at three sites across the Bransfield Strait. Antarctica, *Geophys. Res. Abstr.*, *11*, Abstract EGU2009-13362-1.

Martini, F., C. Bean, G. Saccorotti, F. Viveiros, and N. Wallenstein (2009), Seasonal cycles of seismic velocity variations detected using coda wave interferometry at Fogo volcano, Azores, during 2003–2004, *J. Volcanol. Geotherm. Res.*, *181*, 231–246, doi:10.1016/j.jvolgeores.2009.01.015.

Massa, M., E. Eva, D. Spallarossa, and C. Eva (2006), Detection of earthquake clusters on the basis of waveform similarity, an application in the Monferrato region (Piedmont, Italy), *J. Seismol.*, *10*, 1–22, doi:10.1007/s10950-006-2840-4.

Maurer, H., and N. Deichmann (1995), Microearthquake cluster detection based on waveform similarities, with an application to the western Swiss Alps, *Geophys. J. Int.*, *123*, 588–600, doi:10.1111/j.1365-246X.1995.tb06873.x.

Métaxian, J. P., P. Lesage, and J. Dorel (1997), Permanent tremor of Masaya volcano, Nicaragua: Wave field analysis and source location, *J. Geophys. Res.*, *102*, 22,529–22,545, doi:10.1029/97JB01141.

Métaxian, J. P., P. Lesage, and B. Valette (2002), Locating sources of volcanic tremor and emergent events by seismic triangulation: Application to Arenal volcano, Costa Rica, *J. Geophys. Res.*, *107*(B10), 2243, doi:10.1029/2001JB000559.

Mora, M. M., P. Lesage, B. Valette, G. E. Alvarado, C. Leandro, J. P. Métaxian, and J. Dorel (2006), Shallow velocity structure and seismic site effects at Arenal volcano, Costa Rica, *J. Volcanol. Geotherm. Res.*, *152*, 121–139, doi:10.1016/j.jvolgeores.2005.09.013.

Musumeci, C., S. Gresta, and D. Malone (2002), Magma system recharge of Mount St. Helens from precise relative hypocenter location of microearthquakes, *J. Geophys. Res.*, *107*(B10), 2264, doi:10.1029/2001JB000629.

Ocaña, E., D. Stich, E. Carmona, F. Vidal, M. Bretón, M. Navarro, and A. García-Jerez (2008), Spatial analysis of the La Paca, SE Spain, 2005 seismic series through the relative location of multiplets and principal component analysis, *Phys. Earth Planet. Inter.*, *166*, 117–127, doi:10.1016/j.pepi.2007.12.005.

Ortiz, R., et al. (1997), Monitoring of the volcanic activity of Deception Island, South Shetland island, Antarctica (1986–1995), in *The Antarctic Region: Geological Evolution and Process*, edited by C. A. Ricci, pp. 1071–1076, Terra Antarct., Siena, Italy.

Palo, M., J. M. Ibáñez, M. Cisneros, M. Bretón, E. Del Pezzo, E. Ocaña, J. Orozco-Rojas, and A. M. Posadas (2009), Analysis of the seismic wavefield properties of volcanic explosions at Volcán de Colima, México: Insights into the source mechanism, *Geophys. J. Int.*, *177*, 1383–1398, doi:10.1111/j.1365-246X.2009.04134.x.

Pandolfi, D., C. J. Bean, and G. Saccorotti (2006), Coda wave interferometric detection of seismic velocity changes associated with the 1999 M = 3.6 event at Mt. Vesuvius, *Geophys. Res. Lett.*, *33*, L06306, doi:10.1029/2005GL025355.

Paredes, C., R. Pérez-López, J. L. Giner-Robles, R. De la Vega, A. García-García, and P. Gumiel (2006), Distribución especial y zonificación tectónica de los morfolineamientos en la Isla Decepción (Shetland del Sur, Antártida), *Geogaceta*, *39*, 75–78.

Pelayo, A. M., and D. A. Wiens (1989), Seismotectonics and relative plate motions in the Scotia Sea region, *J. Geophys. Res.*, *94*(B6), 7293–7320, doi:10.1029/JB094iB06p07293.

Poupinet, G., W. L. Ellsworth, and J. Frechet (1984), Monitoring velocity variations in the crust using earthquakes doublets: An application to the Calaveras fault, California, *J. Geophys. Res.*, *89*, 5719–5731, doi:10.1029/JB089iB07p05719.

Press, W. H., B. P. Flannery, S. A. Teukolsky, and W. T. Vetterling (1989), *Numerical Recipes in FORTRAN*, Cambridge Univ. Press, Cambridge, U. K.

Ratdomopurbo, A., and G. Poupinet (1995), Monitoring a temporal change of seismicity velocity in a volcano, application to the 1992 eruption of Mt. Merapi (Indonesia), *Geophys. Res. Lett.*, *22*, 775–778, doi:10.1029/95GL00302.

Rey, J., L. Somoza, and J. Martínez-Frías (1995), Tectonic, volcanic, and hydrothermal event sequence on Deception Island (Antarctica), *Geo Mar. Lett.*, *15*, 1–8, doi:10.1007/BF01204491.

Robertson Maurice, S. D., D. A. Wiens, P. J. Shore, E. Vera, and L. M. Dorman (2003), Seismicity and tectonics of the South Shetland Islands and Bransfield Strait from a regional broadband seismograph deployment, *J. Geophys. Res.*, *108*(B10), 2461, doi:10.1029/2003JB002416.

Ruiz, M., O. Gaspà, J. Gallart, J. Díaz, J. A. Pulgar, J. García-Sansegundo, C. López-Fernández, and J. M. Gonzalez-Cortina (2006), Aftershocks series monitoring of the September 18, 2004 M = 4.6 earthquake at the western Pyrenees: A case of reservoir-triggered seismicity? *Tectonophysics*, *424*, 223–243, doi:10.1016/j.tecto.2006.03.037.

Saccorotti, G., J. Almendros, E. Carmona, J. M. Ibáñez, and E. Del Pezzo (2001a), Slowness anomalies from two dense seismic arrays at Deception Island Volcano, Antarctica, *Bull. Seismol. Soc. Am.*, *91*, 561–571, doi:10.1785/0120000073.

Saccorotti, G., R. Maresca, and E. Del Pezzo (2001b), Array analyses of seismic noise at Mt. Vesuvius Volcano, Italy, *J. Volcanol. Geotherm. Res.*, *110*, 79–100, doi:10.1016/S0377-0273(01)00204-9.

Saccorotti, G., E. Carmona, J. M. Ibáñez, and E. Del Pezzo (2002), Spatial characterization of Agrón, southern Spain, 1988–1989 seismic series, *Phys. Earth Planet. Inter.*, *129*, 13–29, doi:10.1016/S0031-9201(01)00203-5.

Saccorotti, G., L. Zuccarello, E. Del Pezzo, J. M. Ibañez, and S. Gresta (2004), Quantitative analysis of the tremor wavefield at Etna Volcano, Italy, *J. Volcanol. Geotherm. Res.*, *136*, 223–245, doi:10.1016/j.jvolgeores.2004.04.003.

Scarfì, L., H. Langer, and S. Gresta (2003), High-precision relative locations of two microearthquakes clusters in Southeastern Sicily, Italy, *Bull. Seismol. Soc. Am.*, *93*, 1479–1497, doi:10.1785/0120020146.

Shearer, P. M., J. L. Hardebeck, L. Astiz, and K. B. Richards-Dinger (2003), Analysis of similar event clusters in aftershocks of the 1994 Northridge, California, earthquake, *J. Geophys. Res.*, *108*(B1), 2035, doi:10.1029/2001JB000685.

Shelly, D. R., W. L. Ellsworth, T. Ryberg, C. Haberland, G. S. Fuis, J. Murphy, R. M. Nadeau, and R. Bürgmann (2009), Precise location of San Andreas Fault tremors near Cholame, California using seismometer clusters: Slip on the deep extension of the fault?, *Geophys. Res. Lett.*, *36*, L01303, doi:10.1029/2008GL036367.

Smellie, J. L. (1988), Recent observations on the volcanic history of Deception Island, South Shetland Islands, *Br. Antarct. Surv. Bull.*, *81*, 83–85.

Smellie, J. L., and J. López-Martínez (2000), Geological map of Deception Island, *BAS GEOMAP Series*, sheet 6-A, scale 1:25,000, Br. Antarct. Surv., Cambridge, U. K.

Snieder, R., and M. Hagerty (2004), Monitoring change in volcanic interiors using coda wave interferometry: Application to Arenal Volcano, Costa Rica, *Geophys. Res. Lett.*, *31*, L09608, doi:10.1029/2004GL019670.

Stich, D., G. Alguacil, and J. Morales (2001), The relative location of multiplets in the vicinity of the western Almeria (southern Spain) earthquake series of 1993–94, *Geophys. J. Int.*, *146*, 801–812, doi:10.1046/j.0956-540x.2001.01498.x.

Tsujiura, M. (1983), Characteristics frequencies for earthquake families and their tectonic implications, evidences from earthquake swarm in the Kanto District, Japan, *Pure Appl. Geophys.*, *121*, 573–600, doi:10.1007/BF02590156.

Valenzuela, E., B. L. Chavez, and V. F. Munizaga (1968), Informe preliminar sobre la erupción de Isla Decepción ocurrida en Diciembre de 1967, *Bol. Inst. Antart. Chileno*, *3*, 5–16.

Vila, J., J. Martí, R. Ortiz, A. García, and A. M. Correig (1992), Volcanic tremors at Deception Island (South Shetland Islands, Antarctica), *J. Volcanol. Geotherm. Res.*, *53*, 89–102, doi:10.1016/0377-0273(92)90076-P.

Vila, J., A. M. Correig, and J. Martí (1995), Attenuation and source parameters at Deception Island (South Shetland Islands, Antarctica), *Pure Appl. Geophys.*, *144*, 229–250, doi:10.1007/BF00878633.

Waite, G. P., and S. C. Moran (2009), Vp Structure of Mount St. Helens, Washington, USA, imaged with local earthquake tomography, *J. Volcanol. Geotherm. Res.*, *182*, 113–122, doi:10.1016/j.jvolgeores.2009.02.009.

Zandomeneghi, D., A. Barclay, J. Almendros, J. M. Ibáñez, W. S. D. Wilcock, and T. Ben-Zvi (2009), The crustal structure of Deception Island Volcano from P wave seismic tomography: Tectonic and volcanic implications, *J. Geophys. Res.*, *114*, B06310, doi:10.1029/2008JB006119.

J. Almendros, E. Carmona, J. M. Ibáñez, and J. A. Peña, Instituto Andaluz de Geofísica, Universidad de Granada, E-18071 Granada, Spain. (ecarmona@ugr.es)